

Molybdenum Carbide Electrocatalyst In Situ Embedded in Porous Nitrogen-Rich Carbon Nanotubes Promotes Rapid Kinetics in Sodium-Metal–Sulfur Batteries

Hongchang Hao,* Yixian Wang, Naman Katyal, Guang Yang, Hui Dong, Pengcheng Liu, Sooyeon Hwang, Jagannath Mantha, Graeme Henkelman, Yixin Xu, Jorge Anibal Boscoboinik, Jagjit Nanda, and David Mitlin*

This is the first report of molybdenum carbide-based electrocatalyst for sulfur-based sodium-metal batteries. MoC/Mo₂C is in situ grown on nitrogen-doped carbon nanotubes in parallel with formation of extensive nanoporosity. Sulfur impregnation (50 wt% S) results in unique triphasic architecture termed molybdenum carbide–porous carbon nanotubes host (MoC/Mo₂C@PCNT–S). Quasi-solid-state phase transformation to Na₂S is promoted in carbonate electrolyte, with in situ time-resolved Raman, X-ray photoelectron spectroscopy, and optical analyses demonstrating minimal soluble polysulfides. MoC/Mo₂C@PCNT–S cathodes deliver among the most promising rate performance characteristics in the literature, achieving 987 mAh g⁻¹ at 1 A g⁻¹, 818 mAh g⁻¹ at 3 A g⁻¹, and 621 mAh g⁻¹ at 5 A g⁻¹. The cells deliver superior cycling stability, retaining 650 mAh g⁻¹ after 1000 cycles at 1.5 A g⁻¹, corresponding to 0.028% capacity decay per cycle. High mass loading cathodes (64 wt% S, 12.7 mg cm⁻²) also show cycling stability. Density functional theory demonstrates that formation energy of Na₂S_x (1 ≤ x ≤ 4) on surface of MoC/Mo₂C is significantly lowered compared to analogous redox in liquid. Strong binding of Na₂S_x (1 ≤ x ≤ 4) on MoC/Mo₂C surfaces results from charge transfer between the sulfur and Mo sites on carbides' surface.

abundance of sulfur. The lower cost and greater availability of sodium as compared to lithium precursors is spurring the incremental focus on Na–S batteries. The traditional high temperature Na–S batteries operating at 300–350 °C comprise the molten electrodes and the solid inorganic β-alumina electrolyte. This mature design is known to have safety issues and a relatively low theoretical energy 760 W h kg⁻¹ (2Na + 3S → Na₂S₃).^[2] Instead, there is a strong incentive to develop room-temperature (RT) Na–S batteries which in principle allow the two-electron reduction of sulfur to Na₂S, with a higher theoretical energy of 1273 Wh kg⁻¹ and less of a safety concern.^[3]

In practice, RT Na–S cells are likewise held back by several primary challenges including polysulfide (Na₂S_x, 4 ≤ x ≤ 8) dissolution and crossover in liquid electrolytes. Other concerns are the insulating nature of sulfur (σ_e = 5 × 10⁻³⁰ S cm⁻¹) and associated sluggish sulfur redox kinetics, as well as the large volume expansion


(170%) of the cathode on cell discharge.^[4] Sodium ions have lower solid-state diffusivity and reactivity with solid S than lithium ions. Consequently the electrochemical redox processes in Na–S are more sluggish than in the Li–S counterpart.^[5] For Na–S cells, the galvanostatic plateaus are more sloping and less well-defined, while the charge–discharge voltage hysteresis is

1. Introduction

Rechargeable batteries are being widely employed in a broad range of applications ranging from portable electronics to electric vehicles.^[1] Alkali-metal–sulfur batteries are highly promising due to the favorable technoeconomics and the earth

H. Hao, Y. Wang, H. Dong, P. Liu, D. Mitlin
Materials Science and Engineering Program and Texas Materials
Institute (TMI)
The University of Texas at Austin
Austin, TX 78712-1591, USA
E-mail: haohongchang@utexas.edu; David.Mitlin@austin.utexas.edu
N. Katyal, J. Mantha, G. Henkelman
Department of Chemistry
The University of Texas at Austin
Austin, TX 78712, USA

G. Yang, J. Nanda
Chemical Sciences Division
Oak Ridge National Laboratory
Oak Ridge, TN 37830, USA
S. Hwang, Y. Xu, J. A. Boscoboinik
Center for Functional Nanomaterials
Brookhaven National Laboratory
Upton, NY 11973, USA
Y. Xu
Materials Science and Chemical Engineering Department
Stony Brook University
Stony Brook, NY 11790, USA

 The ORCID identification number(s) for the author(s) of this article can be found under <https://doi.org/10.1002/adma.202106572>.

DOI: 10.1002/adma.202106572

larger.^[6] Taken together, these problems lead to a fast capacity fade in Na–S cells during extended cycling.^[7] To improve the performance, several approaches have been attempted. These include creating porous nanocarbon matrices such as metal–organic frameworks (MOF)-derived porous carbon,^[8] hollow carbon nanospheres,^[9] mesoporous carbon nanotubes.^[10] In addition, several sulfiphilic species such as Fe/Ni/Cu clusters,^[11] MnO₂,^[12] TiO₂,^[13] NiS₂,^[10] MoS₂,^[14] and MoSe₂,^[15] have been engineered as effective electrocatalysts to chemically adsorb polysulfides on their surface and to promote the Na–S redox kinetics. Most often, the fabrication approach for such architectures is based on distinct syntheses steps of pore formation and followed by catalyst loading. N-doped carbon (CN)/Au/S,^[16] S/Co–hollow carbon (HC),^[17] MoS_{2-x}@HC/S,^[18] and other examples of cathode systems^[19] have achieved favorable electrochemical performance using such a sequential host activation–catalyst infiltration method.

Molybdenum carbides have been shown to have great promise in enhancing Li–S battery performance in terms of improved sulfur utilization and extended cycle lifetimes.^[20] For instance, Shi et al. developed a self-standing necklace-like molybdenum carbide embedded in interconnected N-doped carbon nanofibers, and employed Li₂S₆ as catholyte in their system.^[20b] The interconnected conductive carbon network derived from low-cost bacterial cellulose precursor enabled fast electron and ion transport in electrode. Moreover, the embedded ultrafine MoC catalytically promoted their redox conversion. As a result, an extraordinary areal capacity of 12.3 mA h cm⁻² at 0.1C was obtained, with employment of such superior electrode and a quite high areal sulfur loading of 10 mg cm⁻². Likewise, Li et al.'s work on Mo₂C embedded carbon nanofibers demonstrated the multifunctions of Mo₂C in promoting Li–Li₂S₆ reaction kinetics.^[20a] Although the host in those prior arts displayed inconspicuous physical confinement of sulfur due to the limited surface area (<300 m² g⁻¹), the sulfiphilic MoC or Mo₂C could still effectively adsorb the polysulfide species in electrolyte through strong chemical interaction.

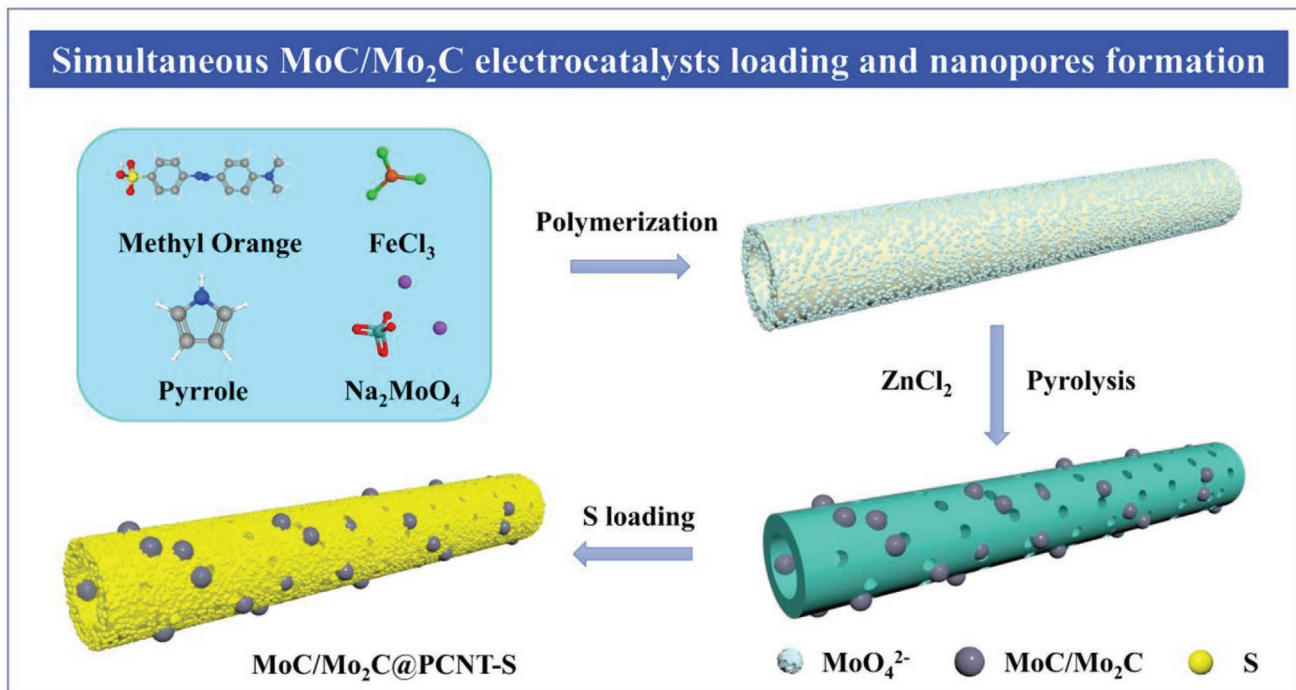
By contrast, the efficacy of molybdenum carbides in Na–S batteries is unexplored. Although much less is known for Na–S as compared to Li–S, the redox reactions with the former are well-documented to be significantly more sluggish, posing a greater challenge for an effective electrocatalyst.^[21] The volume expansion and associated stress of sulfur converting to Na₂S versus to Li₂S (171% vs 80%) create a larger nucleation barrier for the former redox reaction. Sodiation and desodiation reactions are also impeded by the slower solid-state diffusivity of sodium ions within various carbon hosts as compared to lithium ions.^[22] Moreover, the cycling-induced capacity fade with the Na–S systems appears to be more extreme than with Li–S. This is due to a combination of enhanced sodium polysulfide dissolution and possible crossover to the anode, accelerated loss of active S during cycling due to its repeated volume expansion, and because of the instability of the Na-metal anodes in both carbonate and ether electrolytes.^[21,23] In carbonate electrolytes, Na–S batteries may display a “quasi-solid-state phase transformation” where the liquid-phase polysulfide redox reactions are suppressed.^[2,24] This is desirable since it prevents polysulfide dissolution into the electrolyte. To achieve quasi-solid-state reactions with Na–S, the entire redox process has

to be either confined in carbon micropores/small mesopores or to be anchored on energetically favorable secondary surfaces, such as MOF-derived mesoporous carbon,^[25] biomass-derived mesoporous carbon,^[26] sulfur-doped Ti₃C₂T_x MXene nanosheets,^[3] and other hosts. In terms of electrolyte optimization, Na–S performance can be further improved through the addition of fluoroethylene carbonate (FEC) additive, which possesses a lower binding energy with Na polysulfides, and enables polysulfides to remain in the cathode instead of dissolving into electrolyte.^[26,27]

Herein, we report a new approach to significantly promote the Na–S redox kinetics in a sodium-metal battery while in parallel extending its cycling lifetime. The methodology is based in MoC/Mo₂C nanoparticles in situ grown in conjunction with activation of nitrogen-doped hollow porous carbon nanotubes. The novelty lies both in the use of novel molybdenum carbide electrocatalyst, and in the facile single step combined catalyst-formation–host-activation process. The resultant molybdenum carbide–porous carbon nanotubes host (MoC/Mo₂C@PCNT) is rich in micropores and small mesopores, and is able to accommodate a relatively high mass loading (50%) of elemental S. During cycling, the S that is confined in the nanopores and is in contact with the carbides, undergoes a series of rapid and highly reversible reactions to form the terminal Na₂S. A broad comparison with state-of-the-art Na–S literature demonstrates that the MoC/Mo₂C@PCNT–S systems displays a highly promising combination of rate capability and cycling lifetime. Complementary density functional theory (DFT) simulations provide fundamental insight regarding the role of MoC/Mo₂C nanoparticles in promoting the sulfur redox reactions.

2. Results and Discussion

The synthesis strategy for the sulfur host “MoC/Mo₂C@PCNT” is summarized in **Scheme 1**, with extended details of the process being provided in the Supporting Information. Modifying the conventional pyrrole polymerization method, a precursor Na₂MoO₄ was introduced into the reaction scheme. The design rationale was that the negatively charged MoO₄²⁻ anions will strongly interact with the in situ generated polypyrrole through hydrogen bonds and electrostatic forces.^[28] The precipitate of anions azo dye methyl orange and FeCl₃ serves as the complexing template, degrading automatically during the polymerization/growth of pyrrole. The subsequent carbonization process of the Mo-containing polypyrrole nanotubes in the presence of a ZnCl₂ activating agent results in the formation of the final product, MoC/Mo₂C@PCNT. During the high-temperature pyrolysis-activation process, the MoO₄²⁻ species are in situ reduced to the MoC/Mo₂C nanoparticles attached to the nanotubes while nanoporosity is generated. These in situ formed carbides remain stable during the follow-up HCl etching and washing procedure that removes the residual Zn species. Sulfur is impregnated into the nanopores at 50% mass loading to achieve the final cathode material MoC/Mo₂C@PCNT–S. This is done through stepwise melt-infusion at 155 °C first, followed by a heat treatment at 300 °C to remove the residual free sulfur. Baseline materials termed PCNT–S were fabricated through the same procedures except



Scheme 1. Schematic fabrication process and structure of MoC/Mo₂C@PCNT–S composite.

without adding Na₂MoO₄. Figure S1 (Supporting Information) shows thermogravimetric analysis (TGA) results under N₂ atmosphere. The TGA analysis reveals that the sulfur loadings in MoC/Mo₂C@PCNT–S and PCNT–S are 50.3% and 51.8% by weight, respectively.

Analytical characterization of MoC/Mo₂C@PCNT and MoC/Mo₂C@PCNT–S specimens was performed using scanning electron microscopy (SEM) and transmission electron microscopy (TEM). The results for PCNT, MoC/Mo₂C@PCNT, and MoC/Mo₂C@PCNT–S are shown in Figure 1 and in Figures S2–S4 (Supporting Information). The TEM analysis in Figure 1a,b and the SEM analysis in Figures S2 and S3 (Supporting Information) highlight the hollow bamboo-like morphology of PCNTs, with typical diameter in 300 nm range. As per Figure 1c and Figures S2 and S4 (Supporting Information), the MoC/Mo₂C@PCNT composites retain their tubular morphology. As shown in Figure 1c, the carbide nanoparticles are 10–25 nm in diameter and are directly attached to the carbon nanotubes. The high-resolution TEM (HRTEM) images shown in Figure 1e,f reveal that the nanoparticles are encapsulated by several layers of defective graphene, with a dilated lattice spacing of 0.383 nm (vs 0.335 nm for graphite). This has been reported to be caused by the catalytic graphitization of amorphous carbon by the Mo species during the carbonization process.^[29] The graphitic carbon shell provides electrically conductive pathways, while the expanded layer distance allows for insertion/extraction of large sodium ions.^[30] Occasionally, there will be a carbide particle that is lost during sample cleaning and/or specimen preparation, leaving the remanent carbon shell. One such example is illustrated in Figure 1d and is marked by the yellow dotted line. Figure 1f,g shows that the nanoparticles possess a high degree of crystallinity. The lattice

fringes with interplanar spacings of 0.251, 0.230, and 0.175 nm are indexed to the MoC(100), Mo₂C(121), Mo₂C(202) planes, respectively, which are consistent with the indexed selected area electron diffraction (SAED) patterns shown in Figure 1h and Figure S5 (Supporting Information). As demonstrated by energy dispersive X-ray spectroscopy (EDXS) maps shown in Figure 1i, there is a uniform dispersion of S throughout the porous carbon nanotube structure.

The X-ray powder diffraction (XRD) patterns of the PCNT, MoC/Mo₂C@PCNT, and MoC/Mo₂C@PCNT–S samples are shown in Figure 2a. The diffraction profile of MoC/Mo₂C@PCNT shows that the hexagonal MoC (JCPDF no. 45-1015) is the dominant phase within Mo-containing species. The strong peaks at 32.1°, 35.7°, 48.7°, 64.2° are indexed to the corresponding (001), (100), (101), and (110) reflections, respectively. In addition, the relatively weak peak at 39.4° corresponds to the primary (121) reflection of the orthorhombic Mo₂C (JCPDF no. 31-0871). As per X-ray photoelectron spectroscopy (XPS) analysis shown later in the paper, in the MoC/Mo₂C@PCNT composite, the molar ratio of MoC to Mo₂C is 6.25. According to Figure S6 (Supporting Information), the total weight fraction of molybdenum carbides is 14.7 wt%, this result being calculated from TGA test performed in air. Following the sulfur loading process, MoC/Mo₂C@PCNT–S composite does not display crystalline Bragg peaks of S. This is in agreement with it being encapsulated in the nanopores of carbon and hence amorphous. The structure was further analyzed by Raman spectroscopy, as shown in Figure S7 (Supporting Information). The disorder-induced D band at ≈1350 cm⁻¹ and graphitic G band at ≈1580 cm⁻¹ are present in all samples. MoC/Mo₂C@PCNT shows an incrementally higher intensity ratio of G peak to D peak versus the baseline PCNT ($I_G/I_D = 1.0$ vs

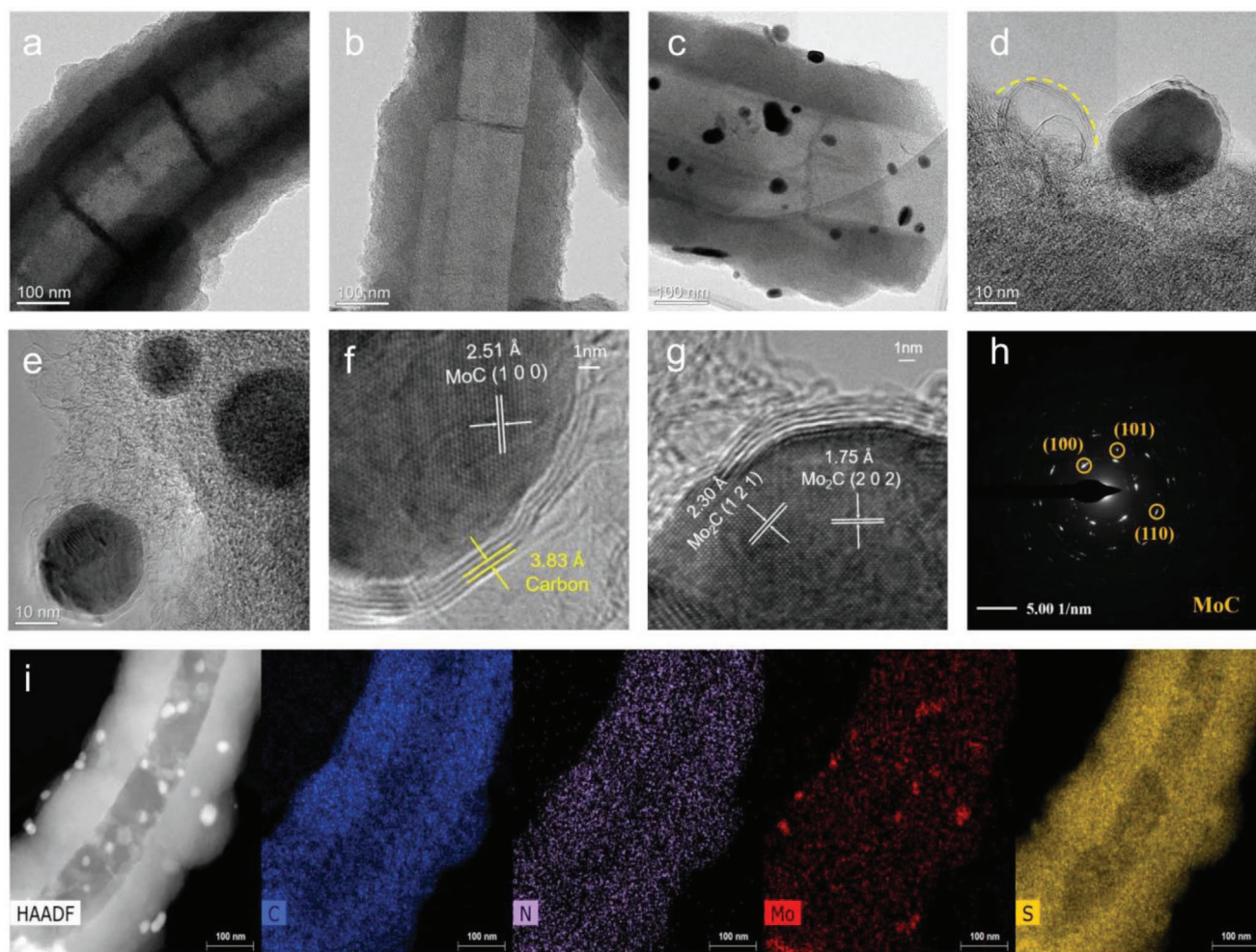


Figure 1. Microstructural characterization of PCNT, MoC/Mo₂C@PCNT, and MoC/Mo₂C@PCNT/S specimens. a,b) HRTEM images of PCNT. c–g) HRTEM images of MoC/Mo₂C@PCNT. h) Indexed SAED of MoC/Mo₂C@PCNT. i) HAADF-STEM image and associated EDXS elemental maps of MoC/Mo₂C@PCNT-S, showing C, N, Mo, and S.

0.9). The catalytic formation of the graphene layers around molybdenum carbide nanoparticles may be responsible for this effect.^[29]

Figure S8 (Supporting Information) displays the indexed XRD patterns of the PCNTs with different loadings of molybdenum. These samples are termed as L-Mo@PCNT and H-Mo@PCNT and were fabricated by changing the initial Na₂MoO₄·2H₂O to pyrrole molar ratios to 1:48 and 1:4, respectively. Within H-Mo@PCNT, the hexagonal MoC likewise dominates with a comparatively lower amount of orthorhombic Mo₂C. As per Figure S9 (Supporting Information), in H-Mo@PCNT, the estimated molar ratio of MoC to Mo₂C is 5. There are no discernable MoC/Mo₂C Bragg peaks in L-Mo@PCNT, indicating that if present, these phases are amorphous or highly nanocrystalline. According to the TGA in air results shown in Figure S6 (Supporting Information), the weight percentage of Mo-containing phases in L-Mo@PCNT and H-Mo@PCNT is 4.5 and 33.2 wt%, respectively.

Nitrogen adsorption/desorption isotherms were employed for a detailed investigation of the textural properties of MoC/Mo₂C@PCNT-S and MoC/Mo₂C@PCNT, as well as of the

PCNT, L-Mo@PCNT, and H-Mo@PCNT. Analyses performed include the calculation of the Brunauer–Emmett–Teller (BET) surface area, as well as of the calculation of the pore size distribution (PSD) based on nonlocal density functional theory (NLDFT) principles. These results are shown in Figure 2b,c as well as in Figure S10 (Supporting Information). The BET specific surface area (S_{BET}), micropore volume (V_{mic}), mesopore volume (V_{mes}), and total pore volume (V_{tot}) are summarized in Table S1 (Supporting Information). The PCNT specimen has a surface area of 1681.0 m² g⁻¹ and a total pore volume of 0.848 cm³ g⁻¹. The MoC/Mo₂C@PCNT specimen displays a surface area of 1249.4 m² g⁻¹ and a total pore volume of 0.645 cm³ g⁻¹. Those values are 1375.6 m² g⁻¹/0.693 cm³ g⁻¹ and 1198.1 m² g⁻¹/0.616 cm³ g⁻¹ for L-Mo@PCNT and H-Mo@PCNT, respectively.

The high surface areas and large pore volumes of these sulfur hosts result from the known role of ZnCl₂ as an effective chemical activation agent. The incorporation of molybdenum carbides reduces the specific surface area and the porosity, while having less impact on the pore size distribution. As per Figure 2b and Figure S10 (Supporting Information), the type IV

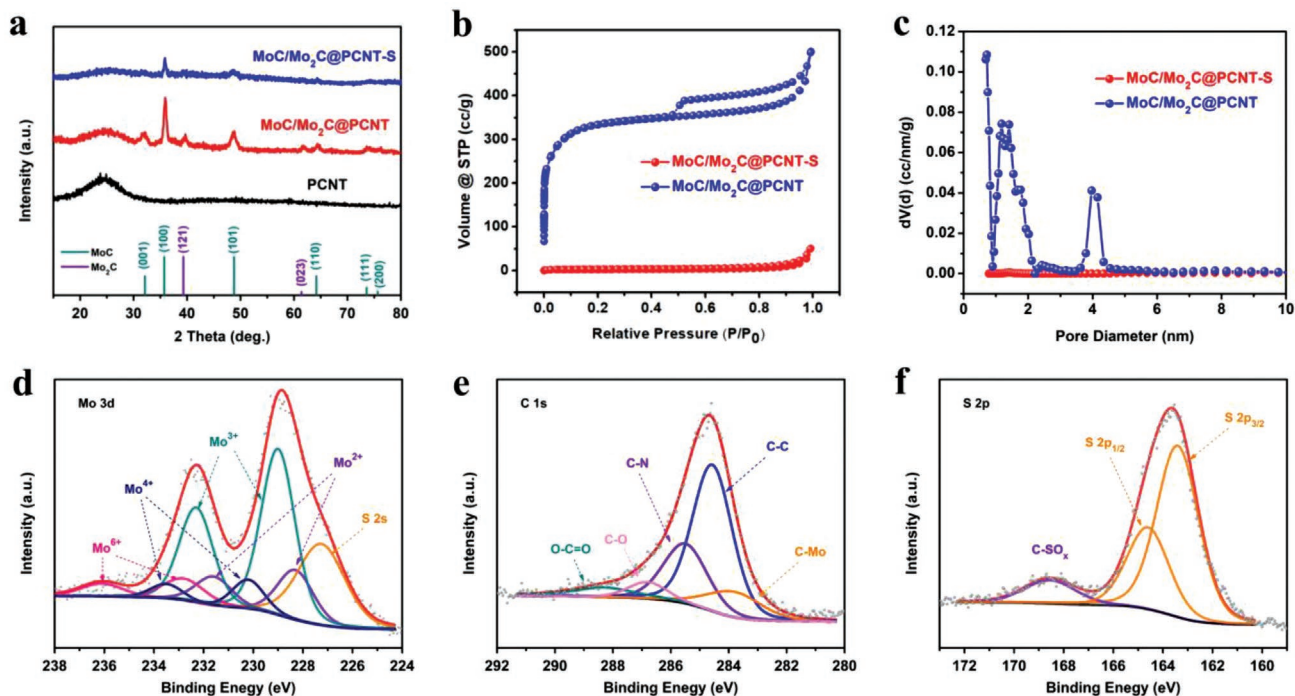


Figure 2. a) Indexed XRD patterns of the prepared PCNT, MoC/Mo₂C@PCNT, and MoC/Mo₂C@PCNT-S. b) Nitrogen adsorption-desorption isotherms and c) NLDFT-derived pore size distributions of MoC/Mo₂C@PCNT-S and MoC/Mo₂C@PCNT. d-f) High-resolution XPS spectra showing Mo 3d, C 1s, and S 2p peaks for the MoC/Mo₂C@PCNT-S composite. The survey spectra and other high-resolution spectra are shown in the Supporting Information.

isotherm along with H4 hysteresis loop at $P/P_0 = 0.5-1.0$ for MoC/Mo₂C@PCNT and other control samples is a typical characteristic of ordered mesoporous materials. All samples show a dramatic increase of N₂ adsorption at $P/P_0 < 0.01$, indicating the presence of micropores. These hosts differ slightly in terms of the V_{mic}/V_{mes} ratio, being 3.96 for PCNT, 4.02 for L-Mo@PCNT, 3.60 for MoC/Mo₂C@PCNT, and 3.85 for H-Mo@PCNT. Figure 2c shows the PSDs for MoC/Mo₂C@PCNT before and after sulfur impregnation, simulated by NLDFT. The sulfur host possesses an average micropore diameter of 1.2 nm and an average mesopore diameter of 4.0 nm. After 50 wt% of S impregnation into the pore cavities, there is minimal porosity available for N₂ adsorption ($0.045 \text{ cm}^3 \text{ g}^{-1}$), and with a concomitant drop in the surface area to $10.714 \text{ m}^2 \text{ g}^{-1}$.

The textural (porosity) properties of the sulfur host can closely determine the reaction pathway of the sulfur.^[31] Micropores are promising reservoirs for accommodating small S molecules and retaining polysulfides.^[32] Experiments by Archer and co-workers showed that when S₈ is confined a carbon with a pore size distribution ranging from 0.6 to 1.8 nm, only insoluble short-chain polysulfide intermediates are formed.^[33] In hosts that are mesoporous, high-order polysulfides (Na₂S_{5.8}) have been reported as well.^[3d,16,17,26,34] Judging from the pore size distribution in MoC/Mo₂C@PCNT, it is reasonable to expect that the MoC/Mo₂C@PCNT-S cathode will undergo a quasi-solid-state reaction with limited involvement of the high-order polysulfide intermediates, agreeing with the overall position of the voltage plateau that is observed experimentally. The prevention of soluble polysulfide species during discharge/charge processes is a key factor determining the cycling stability of Na-S.

XPS was utilized to investigate the chemical states of the elements constituting MoC/Mo₂C@PCNT-S. As per Figure S11 (Supporting Information), characteristic peaks corresponding to S 2p, Mo 3d, C 1s, N 1s, O 1s are observed in XPS survey spectrum. Figure 2d shows the fitted Mo 3d XPS spectrum comprising multiple deconvoluted Mo doublets, and an additional peak assigned to S (2s, 227.0 eV). Two peak doublets located at 228.3, 231.6 and 229.0, 232.3 eV are ascribed to Mo²⁺ and Mo³⁺, respectively.^[29,35] Previous studies have shown that Mo³⁺ is dominant in MoC, whereas Mo²⁺ is intense in Mo₂C.^[36] The areas of deconvoluted Mo³⁺ and Mo²⁺ peaks are capable of providing the molar ratio of MoC to Mo₂C, the value being calculated to be 6.25. Mo⁴⁺ (230.1, 233.4 eV) and Mo⁶⁺ (232.9, 236.2 eV) may originate from the inevitable surface oxidation of molybdenum carbides through air contact. In the C 1s spectrum (Figure 2e), five peaks are present, corresponding to C-Mo (283.9 eV), C-C/C=C (284.6 eV), C-N/C=N (285.5 eV), C-O (286.8 eV), and O-C=O (288.4 eV), respectively. The N 1s XPS spectrum (Figure S11b, Supporting Information) can be deconvoluted into four peaks at 395.0, 398.1, 400.5, and 401.6 eV, which correspond to Mo 3p, pyridinic nitrogen (N-6), pyrrolic nitrogen (N-5), and quaternary nitrogen (N-Q). In S 2p spectrum (Figure 2g), two dominant peaks at 163.4 and 164.2 eV are ascribed to the spin-orbit coupling of elemental S, and the broad peak at 168.7 eV is associated with oxidized-S groups (C-SO_x groups). The XPS results are in overall agreement with the TEM and XRD data.

The electrochemical performances of MoC/Mo₂C@PCNT-S and baseline PCNT-S cathodes were investigated in the voltage window of 0.8–2.8 V. An electrolyte solution of 1 M NaClO₄

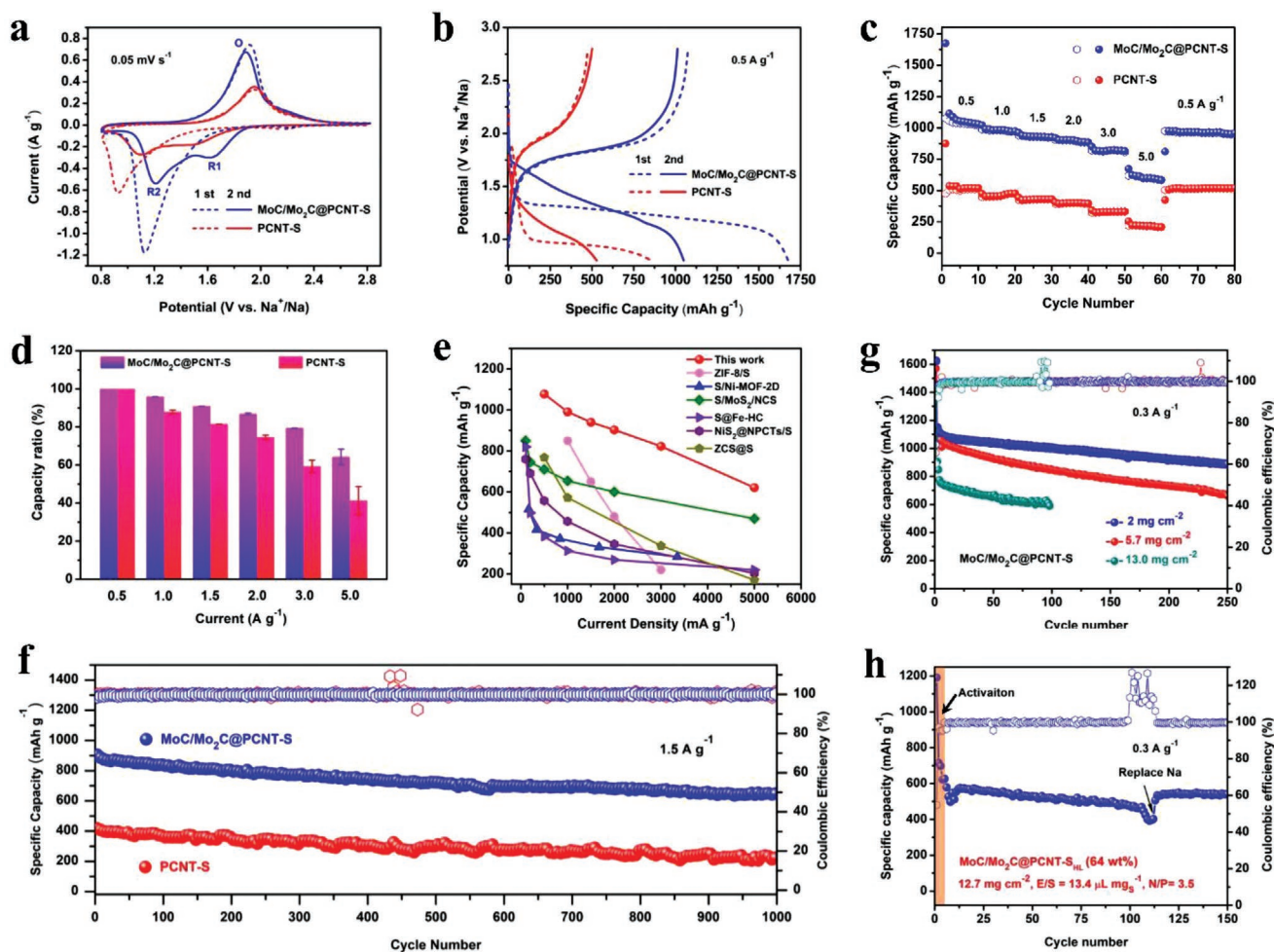


Figure 3. a) CV profiles of MoC/Mo₂C@PCNT-S and baseline PCNT-S electrodes, scanned between 0.8 and 2.8 V at 0.05 mV s⁻¹. b) The first, and the second galvanostatic discharge/charge profiles of MoC/Mo₂C@PCNT-S and baseline PCNT-S electrodes at 0.5 A g⁻¹. c) Rate performances of MoC/Mo₂C@PCNT-S and baseline PCNT-S. d) Percent capacity retention for 1, 1.5, 2, 3, 5 A g⁻¹ for MoC/Mo₂C@PCNT-S and PCNT-S, relative to their respective capacity at 0.5 A g⁻¹. e) Comparison of the specific capacity versus current density for MoC/Mo₂C@PCNT-S versus reported Na-S cathodes from the literature. f) Cyclability of MoC/Mo₂C@PCNT-S and PCNT-S at 1.5 A g⁻¹ (initially activated at 0.5 A g⁻¹). g) Cyclability of MoC/Mo₂C@PCNT-S at 0.3 A g⁻¹ with different mass loadings. h) Cyclability of MoC/Mo₂C@PCNT-S_{HL} at 0.3 A g⁻¹ with high mass loading of 12.7 mg cm⁻².

in 1:1 (volume ratio) ethylene carbonate/diethyl carbonate (DEC) with 5 wt% FEC was employed. An areal mass loading of 2.0 mg cm⁻² was employed, corresponding to a theoretical capacity of 1.17 mAh cm⁻² (based on mass of S). **Figure 3a** compares the first two cyclic voltammogram (CV) curves of MoC/Mo₂C@PCNT-S and PCNT-S at a scan rate of 0.05 mV s⁻¹. The barely discernable reduction peak centered around 2.2 V during the initial cathodic scan can be ascribed to the irreversible reduction of unencapsulated S₈ to long-chain sodium polysulfides Na₂S_x (4 < x ≤ 8), which subsequently suffer from either dissolution or parasitic reaction with carbonate solvent.^[3d] For both materials, this peak's overall intensity is minimal, indicating that the vast majority of the S is incorporated into the carbon pores rather than being left in its free state. The following sharp peak (at 1.15 V for MoC/Mo₂C@PCNT-S and at 0.95 V for PCNT-S), corresponds to the formation of the solid electrolyte interphase (SEI) layer as well as Na₂S₂ and Na₂S compounds.^[37] This combination is termed electrochemical activation. It is highly probable that the observed several layer

dilated graphene sheath around the carbides is exfoliated and broken apart by the sodium ions during the activation process as well. This would allow the particles to be electrocatalytically active during cycling.

The fact that this reduction peak occurs at a higher voltage for MoC/Mo₂C@PCNT-S is indicative of the catalytic nature of the MoC/Mo₂C phases, not only for the reversible reduction of S but also for irreversible SEI formation. The shape of the CV profiles for both electrodes agree with prior reports for a quasi-solid-state mechanism that includes the formation of a protective SEI layer.^[2,8c,32,38] The SEI complements the role of micropores and mesopores in preventing direct contact of the electrolyte solution with the soluble sodium polysulfides intermediates.^[39] After first scan, the cycle 1 cathodic peaks disappear, while two new peaks appear over the following cycles (Figure 3a and Figure S12 (Supporting Information)). The first cathodic peak (termed as R1) is centered at 1.64 V for MoC/Mo₂C@PCNT-S and at 1.5 V for PCNT-S. It has been reported to be due to formation of short-chain sodium

polysulfides Na_2S_x ($2 \leq x \leq 4$).^[8c,32,39a] The second cathodic peak (termed as R2) centers at 1.22 V for MoC/Mo₂C@PCNT-S and at 1.08 V for PCNT-S. It is associated with the transformation of $\text{Na}_2\text{S}_{4-2}$ to Na_2S .^[33,39a] Given nearly identical S mass loading in both electrodes, the markedly higher total current with MoC/Mo₂C@PCNT-S signals greater S utilization, an effect that is directly attributable to the presence of the MoC/Mo₂C electrocatalyst.

Figure 3b shows cycle 1 and cycle 2 galvanostatic profiles for MoC/Mo₂C@PCNT-S and PCNT-S, both tested at 0.5 A g⁻¹. The differences in the positions (all sloping) of the 1st cycle cathodic plateau and in the 2nd cycle reversible cathodic and anodic plateaus for MoC/Mo₂C@PCNT-S versus PCNT-S are consistent with what was observed for the CV profiles. The corresponding hysteresis (taken at the plateau voltage in half-way point) gives a measure of the relative kinetic difficulty for the redox processes for MoC/Mo₂C@PCNT-S versus the baseline. At cycle 2, the MoC/Mo₂C@PCNT-S displays a hysteresis of 0.52 V, while PCNT-S has a hysteresis of 0.91 V. Figure S13 (Supporting Information) displays the galvanostatic curves for both materials at higher current densities. It may be observed that the hysteresis for MoC/Mo₂C@PCNT-S is consistently lower than for PCNT-S. At current densities of 1.0, 1.5, 2.0, 3.0, 5.0 A g⁻¹, the hysteresis for MoC/Mo₂C@PCNT-S is 0.7, 0.81, 0.89, 1.08, 1.31 V. At the same current densities, these values for PCNT-S are 0.98, 1.01, 1.07, 1.12, 1.33 V.

Figure 3c compares the reversible capacities of the two cathodes at various current densities ranging from 0.5 to 5.0 A g⁻¹. At 0.5 A g⁻¹, the MoC/Mo₂C@PCNT-S electrode shows a cycle 1 discharge capacity of 1675 mAh g⁻¹ and a corresponding charge capacity of 1078 mAh g⁻¹. This corresponds to a Coulombic efficiency (CE) of 64.4%. By contrast, the PCNT-S electrode delivers a lower cycle 1 CE value of 54.3%, with a reversible capacity of only 475 mA h g⁻¹. This indicates that PCNT-S likely possesses more unconfined or weakly bound sulfur, that dissolves into electrolyte and thus becomes irreversible. As will be shown by the DFT simulations, MoC/Mo₂C provides strong binding of the Na_2S_x ($1 \leq x \leq 4$) to its surface, which should in turn promote improved utilization and higher initial CE. The MoC/Mo₂C@PCNT-S electrode shows the superior sulfur utilization, achieving 1076, 987, 939, 903, 818, 621 mAh g⁻¹ at 0.5, 1.0, 1.5, 2.0, 3.0, 5.0 A g⁻¹, respectively. By contrast, PCNT-S delivers 503, 447, 425, 394, 323, 222 mAh g⁻¹ at these current densities. After testing at high currents and reverting back to 0.5 A g⁻¹, a reversible capacity of 977 mAh g⁻¹ is obtained with MoC/Mo₂C@PCNT-S. This demonstrates that the electrode can endure high-rate testing without degrading its structure so as to negatively affect the lower rate redox kinetics. The L-Mo@PCNT-S and H-Mo@PCNT-S cathodes were also tested, as per Figure S14 (Supporting Information). It may be observed that L-Mo@PCNT-S displays inferior rate performance (e.g., 443 mAh g⁻¹ at 5.0 A g⁻¹) and cycling stability as compared to MoC/Mo₂C@PCNT-S. This may be straightforwardly attributed to an inadequate electrocatalyst loading. The H-Mo@PCNT-S specimen displays a comparable rate capability to MoC/Mo₂C@PCNT-S, achieving 623 mAh g⁻¹ at 5.0 A g⁻¹. Its retained capacity after 250 cycles at 1.5 A g⁻¹ is lower than that for MoC/Mo₂C@PCNT-S, being 686 versus 794 mAh g⁻¹. The inferior cycling stability may be attributed to

the excessive mass loading of the carbides that may cause catalyst agglomeration and/or block the fast diffusion of sodium in and out of the microstructure.

The rate performance of MoC/Mo₂C@PCNT-S and PCNT-S baseline was further analyzed in relative terms, considering the percent reduction of reversible capacity with increasing current relative to the 0.5 A g⁻¹ value. For each material, two sets of cathodes were assembled and tested identically. The corresponding electrochemical performances are shown in Figure S15 (Supporting Information) and are analyzed in combination with the data from Figure 3c. Figure 3d plots the two specimen-averaged percentages for 1, 1.5, 2, 3, 5 A g⁻¹ currents, with error bars included. The results demonstrate that MoC/Mo₂C@PCNT-S not only retains a higher reversible capacity at each current, but also a higher fraction of the low current capacity. For MoC/Mo₂C@PCNT-S, the capacity retention is 95.8%, 90.9%, 86.9%, 79.3%, 64.2% of the 0.5 A g⁻¹ value at 1, 1.5, 2, 3, 5 A g⁻¹ currents, respectively. For PCNT-S, these values are 87.8%, 81.5%, 74.5%, 59.2%, and 41.2% of the 0.5 A g⁻¹ value at 1, 1.5, 2, 3, 5 A g⁻¹ currents, respectively. Figure 3e and Table S2 (Supporting Information) present a rate capability comparison of MoC/Mo₂C@PCNT-S with state-of-the-art sulfur-carbon cathodes from the published literature. It may be observed that the rate capability of MoC/Mo₂C@PCNT-S is among favorable. To exclude capacity contribution from the S host, the MoC/Mo₂C@PCNT and PCNT electrodes were also tested against Na between 0.8 and 2.8 V. As shown in Figure S16 (Supporting Information), the sulfur-free hosts show negligible reversible capacities.

The MoC/Mo₂C@PCNT-S electrode was then tested for prolonged cycling lifetime, the results being shown in Figure 3f. After the initial SEI formation and other activation processes, MoC/Mo₂C@PCNT-S delivers a high reversible capacity of 905 mAh g⁻¹ at 1.5 A g⁻¹, retaining 650 mA h g⁻¹ after 1000 cycles. This is equal to overall 72% capacity retention and 0.028% capacity decay per cycle. As per the comparison presented in Table S2 (Supporting Information), MoC/Mo₂C@PCNT-S shows highly promising extended cycling lifetime and retained capacity. The corresponding galvanostatic discharge/charge profiles are consistently stable throughout the duration of cycling, as shown in Figure S17 (Supporting Information). By contrast, PCNT-S retains only 230 mAh g⁻¹ after 1000 cycles, corresponding to a capacity retention of 55%. The faster capacity decay for PCNT-S is due to a combination of Na_2S_x dissolution and low utilization efficiency.

Polysulfide crossover is known to be more pronounced when testing at lower current densities since there is more time for liquid-phase diffusion at every cycle.^[40] According to Figure 3g and Figure S18a (Supporting Information), at 0.3 A g⁻¹, the MoC/Mo₂C@PCNT-S cathode achieves a reversible capacity of 888 mA h g⁻¹ after the 250 cycles, corresponding to a capacity retention of 77%. Such promising cycling stability at low current is a good indicator for the capability of the MoC/Mo₂C@PCNT-S architecture in preventing polysulfide dissolution and crossover, the fundamental origins for this effect being examined by DFT later in the paper. To further probe polysulfide dissolution, postmortem analysis was performed on the separator, the sulfur cathode, and Na-metal anode after cycling at different conditions. A cell with PCNT-S baseline

cathode was cycled for 25 cycles at 0.3 A g⁻¹. A cell with MoC/Mo₂C@PCNT-S cathode was cycled for 25 cycles at 0.3 A g⁻¹. Another cell with MoC/Mo₂C@PCNT-S cathode was cycled for 100 cycles at 1.5 A g⁻¹. Figure S19 (Supporting Information) displays the postmortem analysis on the separator and the anode cycled under these conditions. Figure S19a,d,g (Supporting Information) displays a photograph of the extracted separator, the SEM image of Na anode, and the corresponding elemental map of sulfur obtained from the Na-S cell with PCNT-S cathode after 25 cycles at 0.3 A g⁻¹. Figure S19b,e,h (Supporting Information) shows these results for the MoC/Mo₂C@PCNT-S cell after 25 cycles at 0.3 A g⁻¹, while Figure S19c,f,i (Supporting Information) displays the results for 100 cycles at 1.5 A g⁻¹. The separator extracted from PCNT-S cell is yellow in color on both of its sides, which is an established indicator for having polysulfides dissolved into the electrolyte. The corresponding cycled Na-metal electrode is covered by S species, as per the strong S EDXS signal originating from its surface. By contrast, the separator employed with MoC/Mo₂C@PCNT-S is not yellow, while the S signal from the associated Na anode is much less intense. This further points to the ability of the MoC/Mo₂C to suppress polysulfide dissolution.

Figure S20 (Supporting Information) displays TEM and HRTEM images of the MoC/Mo₂C@PCNT-S after 25 cycles at 0.3 A g⁻¹. Figure S21 (Supporting Information) displays high-angle annular dark-field scanning transmission electron microscopy (HAADF-STEM) images and EDXS maps of the MoC/Mo₂C@PCNT-S after 25 cycles at 0.3 A g⁻¹. Figure S22 (Supporting Information) shows TEM and HRTEM images and indexed SAED of the MoC/Mo₂C@PCNT-S composite after 100 cycles at 1.5 A g⁻¹. Figure S23 (Supporting Information) gives the HAADF-STEM images and EDXS maps of the MoC/Mo₂C@PCNT-S composite after 100 cycles at 1.5 A g⁻¹. It may be observed that the structure and the overall morphology of MoC/Mo₂C nanoparticles in the carbon matrix are preserved throughout cycling. There is little evidence of kinetics-decay inducing changes such as pulverization, agglomeration, or coverage by insulating “free” Na₂S or S. Since the discharge voltage is below 1.5 V versus Na/Na⁺, the electrode surface is covered by a uniform SEI layer. It is mainly composed of O, and F-containing species, as indicated by the EDXS maps in Figures S21 and S23 (Supporting Information).

The electrochemical performance of MoC/Mo₂C@PCNT-S and PCNT-S was also evaluated at 50 °C. The results are shown in Figure S24 (Supporting Information). At elevated temperatures, the sulfur redox kinetics can be improved due to a number for electrolyte- and electrode-related factors.^[41] However, higher temperature also accelerates polysulfide dissolution into the electrolyte.^[40,42] As shown in Figure S24d (Supporting Information), PCNT-S displays an initial discharge capacity of 722 mAh g⁻¹ at 0.3 A g⁻¹, with the plateau at 2.1 V being associated with long-chain polysulfide formation. There is negligible reversible capacity afterward, likely because the active sulfur is now dissolved into electrolyte.^[7a] By contrast, MoC/Mo₂C@PCNT-S delivers an initial discharge capacity of 1847 mAh g⁻¹ at 0.3 A g⁻¹, and a corresponding charge capacity of 967 mAh g⁻¹. After 200 cycles at 1.5 A g⁻¹, a reversible capacity of 401 mAh g⁻¹ is still obtained as per Figure S24a (Supporting Information). The comparison of electrochemical

performance at 50 °C further demonstrates that the dissolution of polysulfides is inhibited by MoC/Mo₂C.

High mass loading cathodes were tested to ascertain the utility of the MoC/Mo₂C@PCNT-S for near commercial applications. As per Figure 3g, the electrode with a loading of 5.7 mg cm⁻² (equal to 2.0 mg S cm⁻²) displays an initial discharge capacity of 1570 mAh g⁻¹ and an initial charge capacity of 1028 mAh g⁻¹ at 0.3 A g⁻¹, corresponding to an initial CE of 65.4%. This is equal to a reversible areal capacity as high as 2.1 mAh cm⁻², and after 250 cycles, a high capacity of 1.32 mAh cm⁻² (660 mAh g⁻¹) is still retained. The corresponding galvanostatic discharge/charge profiles are shown in Figure S18b (Supporting Information), being stable and well-defined throughout the duration of cycling. The cell with higher cathode loading up to 13.0 mg cm⁻² (equal to 4.6 mg S cm⁻²) can still give a reversible capacity of 754 mAh g⁻¹ (3.5 mAh cm⁻²) at the same rate, and stably run for 80 cycles. The MoC/Mo₂C@PCNT-S cathode with a high mass loading of 4.2 mg cm⁻² also underwent long cycling at 1.5 A g⁻¹. Those cycling results are shown in Figure S25 (Supporting Information). After activation, the cell delivers a reversible capacity as high as 804 mAh g⁻¹, corresponding to an areal capacity of 1.2 mAh cm⁻². This further substantiates the superior sulfur redox kinetics and the robustness of the MoC/Mo₂C@PCNT-S composite. It is especially the case considering that this fast charge/discharge rate is associated with the same drastic volume change of 170 vol% due to the S to Na₂S transformation. At such harsh conditions, the cell displays a quite low capacity decay rate of 0.045% per cycle over 1000 cycles. As per Table S2 (Supporting Information), these values are above most previously reported areal capacities, which are below 0.8 mAh cm⁻².

The MoC/Mo₂C@PCNT-S_{HL} with higher S mass loading of 64.0 wt% was prepared. The S loading was confirmed by TGA analysis, shown in Figure S26a (Supporting Information). Such high loading is beyond the maximum theoretical S loading of 57.2 wt%, as calculated from the pore volume of the host. Accordingly, the XRD pattern of MoC/Mo₂C@PCNT-S_{HL} shows the characteristic peaks corresponding to crystalline S. Those results are shown in Figure S26b (Supporting Information) and indicate that some of the impregnated S remained outside the nanopore confines. A quite high mass loading of 12.7 mg cm⁻² (5.7 mg S cm⁻²) was employed in the Na-S cell. This corresponds to an electrolyte-to-sulfur (E/S) ratio of 13.4 μL mg⁻¹ and a negative/positive (N/P) areal capacity ratio of 3.5. As shown in Figure 3h, following stepwise electrochemical activation (3 cycles at 0.05 A g⁻¹ followed by 2 cycles at 0.2 A g⁻¹), the cell was cycled at 0.3 A g⁻¹. A reversible capacity of 576 mAh g⁻¹ is obtained at cycle 10, and the cell stably runs for around 100 cycles. After that, the capacity suddenly drops, while the CE begins to fluctuate (Figure S27, Supporting Information). It is known that a severely fluctuating CE and impedance rise prior to cell failure is associated with unstable SEI and “dead metal” on the Na anode.^[23,43] Such failure mode is more severe when the anode is deeply stripped/plated,^[43b] as is the case here due to the active mass loading of the cathode. To illustrate this point, the MoC/Mo₂C@PCNT-S_{HL} cell was disassembled in a glove box with the degraded Na anode being replaced with a fresh foil. The point where the test was interrupted to do this is marked in the figure. After anode replacement, the stability

of MoC/Mo₂C@PCNT-S_{HL} cell is improved, with the reversible capacity recovering to 549 mAh g⁻¹ (3.13 mAh cm⁻²). When switching out the anode and reassembling the cell, the cathode was not modified in any way. The recovery in the capacity is then associated with renewed ability of the anode to match the cathode's capacity during the plating/stripping cycles.

Postmortem XPS characterization was employed to analyze the electrodes at different electrochemical states. The electrode was first run for 1 cycle at 0.3 A g⁻¹ to accomplish SEI formation and sulfur activation, and then was discharged or charged to different stages for XPS analysis. To avoid the oxidation-related artifacts, the disassembling, solvent (DEC) rinse, and transfer steps were carried out in an inert Ar atmosphere glove box. Figure 4a shows the high-resolution S 2p XPS spectra of the MoC/Mo₂C@PCNT-S electrodes. At an intermediate sodiation state at 1.4 V, the pristine peak doublets (163.4, 164.2 eV) assigned to elemental S disappear. What is present instead are two deconvoluted doublets at 161.2/162.4 and 159.4/160.6 eV, representing Na₂S_x (2 ≤ x ≤ 4) and Na₂S, respectively.^[3a,8c,33,44]

The absence of the specific peaks corresponding to long-chain sodium polysulfides (should be at 164.0 eV),^[14] indicates that sulfur is directly transformed to short-chain polysulfides (Na₂S₄₋₂).^[45] In the terminally sodiated state at 0.8 V, the peaks associated with Na₂S₄₋₂ fade in relative intensity, while the Na₂S peak at 159.4/160.6 eV becomes prominent.^[44a] When desodiated to an intermediate voltage of 1.9 V, the majority of S²⁻ and S_x²⁻ (2 ≤ x ≤ 4) species is oxidized back to elemental S. There are no detectable long chain polysulfides in the spectra either. In the fully charged state, the peaks assigned to elemental S are dominant. The minor peaks at 160.7/161.9 eV indicate some residual sulfide species due to a not fully complete oxidation reaction. However, those peak intensities are quite low relatively.

To further probe the quasi-solid-state conversion mechanism with MoC/Mo₂C@PCNT-S, in situ micro-Raman analysis was conducted. Measurements were performed on a glass fiber separator in a dedicated in situ Raman pouch cell assembled at Oak Ridge National Laboratory (ORNL), using the same

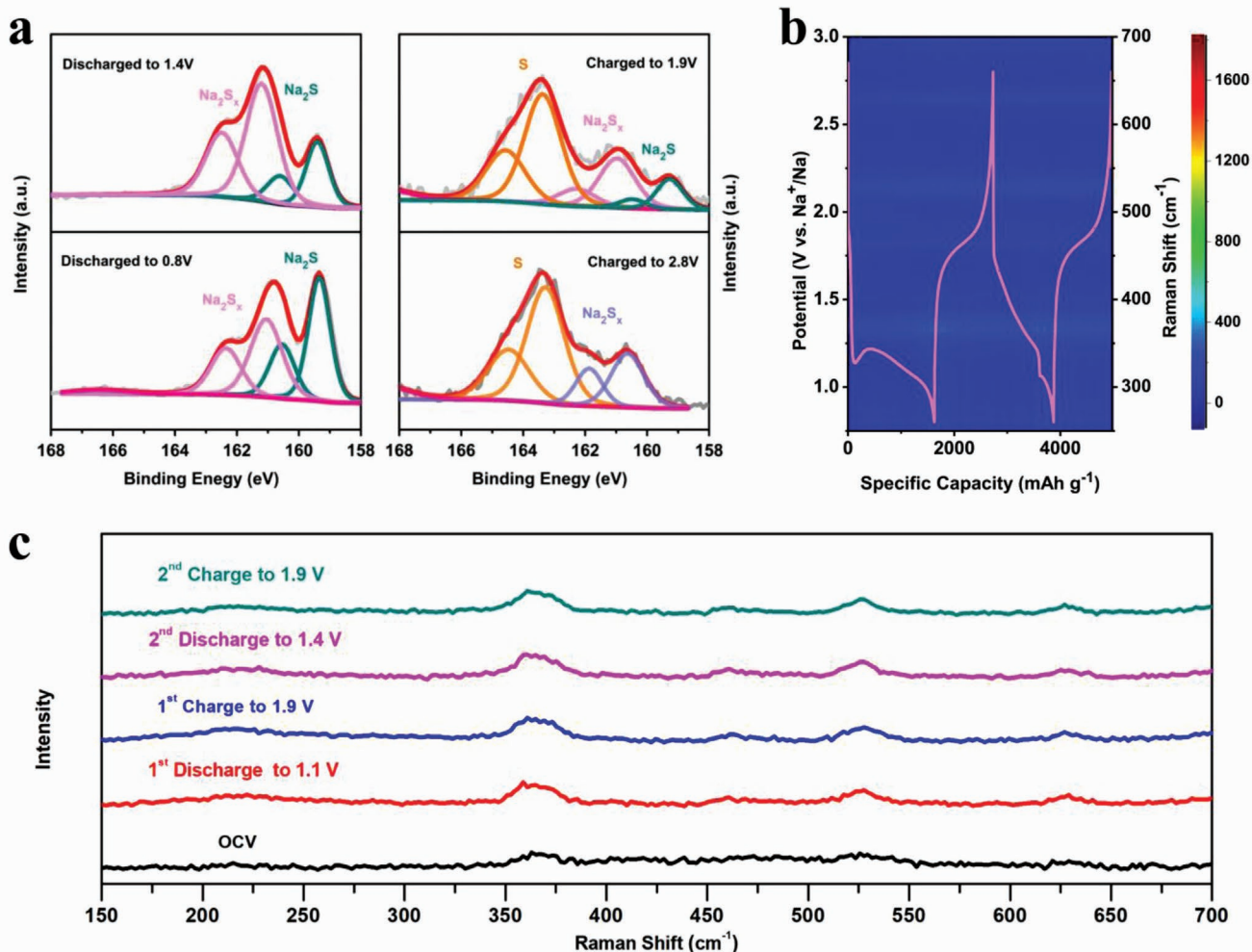


Figure 4. a) High-resolution S 2p XPS spectra of the MoC/Mo₂C@PCNT-S electrodes at different sodiation/desodiation states. Samples were activated at 0.3 A g⁻¹ for 1 cycle and then ramped to designated voltage at the same current density. b) In situ time-resolved Raman image of the glass fiber separator during the cycles 1 and 2, where MoC/Mo₂C@PCNT-S was used as the cathode. The insetted pink curve is the corresponding Na-S voltage profile. c) Selected Raman spectra of the glass fiber separator at different sodiation/desodiation states.

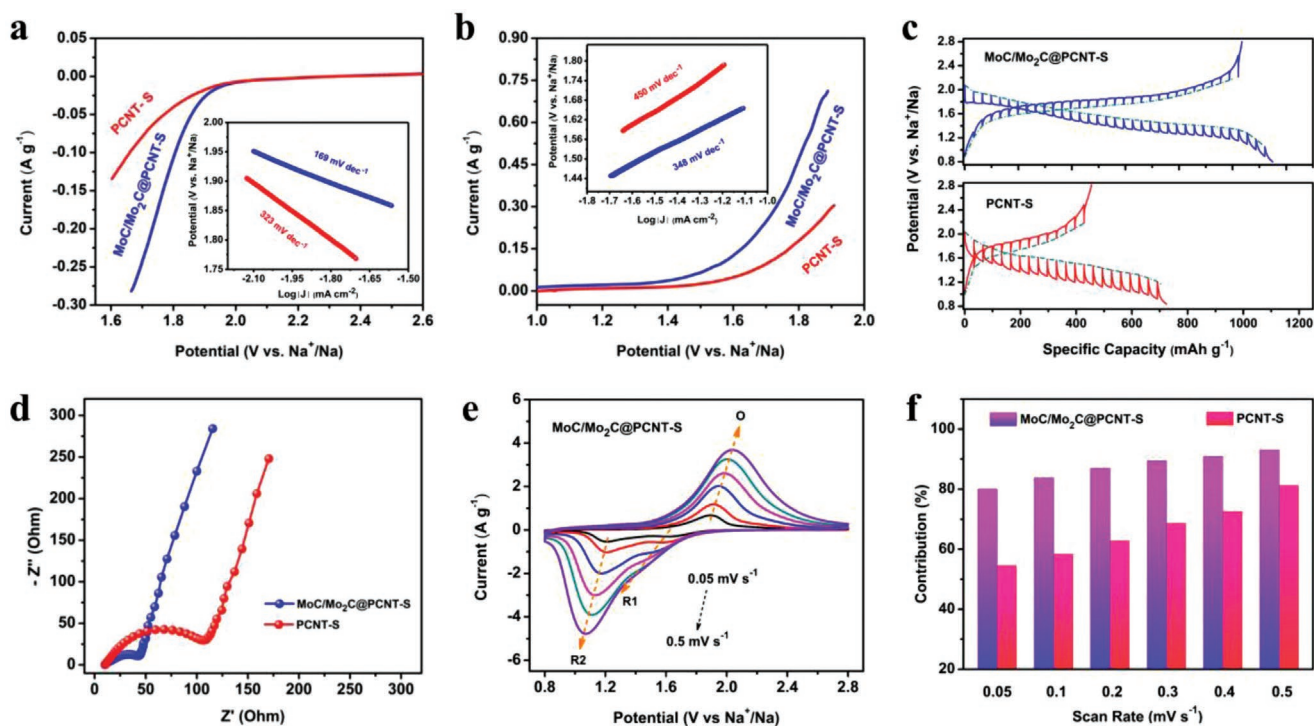


Figure 5. Electroanalytical results comparing MoC/Mo₂C@PCNT-S versus baseline PCNT-S. a) Enlarged cathodic sections of the cycle 2 CV curves, with the derived Tafel plots (inset). b) Enlarged anodic sections of the cycle 2 CV curves, with the derived Tafel plots (inset). c) GITT curves of MoC/Mo₂C@PCNT-S and baseline PCNT-S electrodes at cycle 2. d) EIS Nyquist plots of MoC/Mo₂C@PCNT-S versus PCNT-S electrodes after the initial discharge/charge process. e) CV curves of the MoC/Mo₂C@PCNT-S electrode at various scan rates. f) Reaction-controlled contribution comparison at various scan rates.

electrolyte as the rest of the study. Whether the polysulfides actively dissolve into the electrolyte is indicated by whether their Raman signals are detected on the separator.^[46] If sulfur redox follows a conventional solid-liquid conversion reaction route, some characteristic polysulfide peaks are at 149, 219, and 477 cm⁻¹ for S₈²⁻, 202 and 445 cm⁻¹ for S₄²⁻, 535 cm⁻¹ for S₃^{•-}.^[24,46,47] Figure 4b exhibits the contour plot of Raman spectra recorded from the separator, along with a corresponding galvanostatic profile overlay. Selected Raman spectra at different electrochemical states are shown in Figure 4c. It may be observed that during two cycles of charging and discharging, no peaks appear at the above wavelengths, indicating minimal polysulfides at the separator. Complementary analysis of the electrolyte was performed using a dedicated optically transparent glass cell. Figure S28 (Supporting Information) shows photographs of the optically transparent Na-S cells with the MoC/Mo₂C@PCNT-S electrode, at initial state and cycled for 1, 6, and 24 h at 0.15 A g⁻¹. No obvious color change was observed even after 24 h of continuous discharging/charging. Taken together, those observations demonstrate that sulfur dissolution in the studied ester-based electrolyte system is negligible. The robust F-containing cathode-electrolyte interphase that forms on the cathode during the initial discharging also favors such quasi-solid-state reaction pathway, forming a Na-ion-soluble but polysulfide insoluble sheath around the cathode.

Electroanalytical studies were performed to further understand the role of MoC/Mo₂C catalyst in the sulfur redox kinetics. Figure S29 (Supporting Information) shows the

enlarged cathodic sections of CV curves (0.05 mV s⁻¹) at cycle 1. The MoC/Mo₂C@PCNT-S presents a more positive onset potential for the Na₂S/Na₂S₂/SEI formation as compared to PCNT-S electrode. Accordingly, it displays a lower Tafel slope, being at 374 versus 520 mV dec⁻¹. **Figure 5a,b** compares the sulfur kinetics at cycle 2, where the earlier onset potentials are likewise obtained with MoC/Mo₂C@PCNT-S. As per Figure 5a, MoC/Mo₂C@PCNT-S displayed a lower Tafel slope for the sulfur reduction process to Na₂S₄, being at 169 versus 323 mV dec⁻¹. As shown in Figure 5b, the corresponding Tafel slope for Na₂S/Na₂S₂ oxidation process is also lower with MoC/Mo₂C@PCNT-S, being at 348 versus 450 mV dec⁻¹. The significant reduction in Tafel slopes has been directly correlated with effective electrocatalysis for S redox reactions.^[48]

Galvanostatic intermittent titration technique (GITT) was carried out on MoC/Mo₂C@PCNT-S and PCNT-S electrodes, with 0.5 h current pulse of 83.8 mA g⁻¹ (0.05C) followed by 4 h relaxation. Figure S30 (Supporting Information) shows the potential response profiles of the two electrodes during the initial discharge process, in which the dashed lines represent the equilibrium open-circuit voltages. The MoC/Mo₂C@PCNT-S electrode shows lower overpotentials than PCNT-S, indicative of more facile reaction kinetics.^[49] The plots for the following desodiation and sodiation processes are displayed in Figure 5c, likewise validating the kinetically favorable sulfur redox in MoC/Mo₂C@PCNT-S. The chemical diffusion coefficients of Na⁺ are calculated and shown in Figure S31 (Supporting Information). Overall, the diffusion coefficient values are on

par for MoC/Mo₂C@PCNT-S and PCNT-S electrodes, both in the range of 10⁻⁹ to 10⁻¹¹ cm² s⁻¹. This result indicates that the kinetics enhancement is not associated with a solid-state diffusivity effect.

The electrochemical impedance spectroscopy (EIS) Nyquist plots of two electrodes were analyzed at cycle 1 and after 100 cycles, in the frequency range from 1 MHz to 10 mHz with an amplitude of 10 mV. Those results are plotted in Figure 5d and Figure S32 (Supporting Information). In EIS Nyquist plots, the intercept on the Z'-axis in high-frequency region is the Ohmic resistance (R_{ohm}), associated with combined resistances of the electrode assembly and of the electrolyte. The half-circle represents a combination of SEI resistance (R_{SEI}) and charge-transfer resistance (R_{ct}), the R_{SEI} being at higher frequency.^[50] It is not unusual for the two resistances to overlap sufficiently that they cannot be mathematically deconvolved, as is the case here. Herein, we term the resistance R_{ct} with the implicit recognition that R_{SEI} is included as well. The 45° line in low-frequency region represents the Warburg impedance (Z_w) and is related to solid-state diffusion of Na⁺ in the electrode materials.^[51] After the first sodiation-desodiation cycle, R_{ohm} for MoC/Mo₂C@PCNT-S is 9.8 Ω, and it is 10.5 Ω for PCNT-S. By cycle 100, these values increase slightly to 11.7 and 12.0 Ω, respectively. The more significant difference lies in the R_{ct} values. At cycle 1, the MoC/Mo₂C@PCNT-S electrode displays a lower R_{ct} value than PCNT-S, 51 versus 120 Ω. These results are shown in Figure 5d.

The exchange current density i₀ for sulfur redox is calculated based on the Butler-Volmer equation $i_0 = RT/nFAR_{ct}$, where R is the gas constant, T is the absolute temperature, n is the number of transferred electrons, F is the Faraday constant, and A is the surface area.^[52] The exchange current density is calculated to be 0.3 mA cm⁻² for MoC/Mo₂C@PCNT-S and 0.13 mA cm⁻² for PCNT-S. As per Figure S32 (Supporting Information), the MoC/Mo₂C@PCNT-S still retains a lower R_{ct} value after 100 cycles at 0.5 A g⁻¹, being 114 versus 186 Ω. This is equal to i₀ of 0.14 and 0.08 mA cm⁻² for the MoC/Mo₂C@PCNT-S and the PCNT-S, respectively. The lower charge-transfer impedance of the MoC/Mo₂C@PCNT-S contributes to its fast reaction kinetics and enhanced rate capability. More facile redox kinetics also leads to improved cycling stability since there is less unreacted S at every cycle.

Cyclic voltammetry curves at different scan rates were further employed for the in-depth kinetic analyses. Figure 5e and Figure S33 (Supporting Information) display the CVs of MoC/Mo₂C@PCNT-S and PCNT-S electrodes at increasing sweep rates from 0.05 to 0.5 mV s⁻¹. There is a noticeable shift as the scan rate increases, which is indicative of polarization effects. It is possible to quantitatively analyze the reaction kinetics with respect to the reaction-controlled capacity contribution to the total reversible capacity, based on an established formula, where (i) is the maximum current at a given scan rate (ν): $i(V) = k_1ν + k_2ν^{1/2}$.^[53] A square root time dependence corresponds to a diffusion-controlled process, i.e., concentration polarization. A linear time dependence corresponds to a reaction-controlled process, i.e., activation polarization. This is often termed "surface capacitive process" in the literature.^[54] For high surface area systems that do not form SEI, such as electrochemical capacitors, the surface capacitive process is synonymous with

non-Faradaic electric double-layer capacitor (EDLC) charge storage. However, EDLC charge storage does not apply to either MoC/Mo₂C@PCNT-S or PCNT-S, considering their insufficient electroactive surface area and the SEI. Rather, a linear time dependence indicates a number of surface or bulk reaction-controlled processes that occur during S reduction/oxidation. By plotting $i/ν^{1/2}$ versus $ν^{1/2}$ at a fixed potential, the parameters k₁ and k₂ can be determined, with Figure 5f showing the results. For the MoC/Mo₂C@PCNT-S electrode, the calculated reaction-controlled contribution is as high as 80% even at a low scan rate of 0.05 mV s⁻¹. The reaction-controlled contribution can further increase to 84% at 0.1 mV s⁻¹, 87% at 0.2 mV s⁻¹, 90% at 0.3 mV s⁻¹, 91% at 0.4 mV s⁻¹, and 93% at 0.5 mV s⁻¹. By contrast, the PCNT-S electrode displays overall lower reaction-controlled contribution, which is in the range of 55–81% at the same scan rates. These results are consistent with MoC/Mo₂C@PCNT-S displaying superior rate kinetics during the high current testing.

DFT has been previously employed to calculate the binding energies of different sodium polysulfide molecules on polar and nonpolar hosts to understand electrocatalytic effects.^[3b,55] Here, DFT calculations are made for the formation energy of different short-chain sodium polysulfides (Na₂S_x, 1 ≤ x ≤ 4) on MoC and MoC₂ host structures, and on the baseline PCNT. These values are employed to elucidate the stability of different Na₂S_x species in solid phase or with the implicit solvation model. In order to model the formation energy of sodium polysulfides on MoC/Mo₂C structures, surface energies were calculated for all possible surfaces with Miller index less than or equal to 3 for bulk Mo₂C and MoC. Mo₂C is an orthorhombic structure crystallizing in Pbcn space group, while MoC is a hexagonal structure in the P6m2 space group. The orthorhombic phase of Mo₂C and the hexagonal phase of MoC were considered because these two phases were found to exist in the experimental XRD results. Table S3 (Supporting Information) shows the calculated surface energies of MoC and Mo₂C; the lowest energy (101) surface was selected for binding energy studies on MoC and Mo₂C. For comparison, the graphene surface was also investigated as an approximation to the baseline carbon host. As per $E_{\text{form}} = E_{\text{slab}+\text{Na}_2\text{S}_x} - E_{\text{slab}} - \frac{1}{x} \times E_{\text{Na}_2\text{S}} - \left(1 - \frac{1}{x}\right) \times E_s$, the formation energy for Na₂S_x (1 ≤ x ≤ 4) is taken as the enthalpy change when solid S and Na₂S phases are converted to the Na₂S_x molecules bound to a slab of the cathode host.^[3b] The formation energy of Na₂S_x (1 ≤ x ≤ 4) in the "liquid" and "solid" state was also calculated, both in the absence of solid host substrates. The "liquid" phase refers to the formation energy of free polysulfide molecules inside a box modeled with the implicit solvent. The formation energies of "solid" phases were calculated for Na₂S₄, Na₂S₂, and Na₂S via $E_{\text{form}} = E_{\text{Na}_2\text{S}_x} - \frac{1}{x} \times E_{\text{Na}_2\text{S}} - \left(1 - \frac{1}{x}\right) \times E_s$.

As per Figure 6a, the formation energy of Na₂S_x (1 ≤ x ≤ 4) on MoC/Mo₂C is significantly lowered as compared to value on graphene, which supports the experimental observation that MoC/Mo₂C@PCNT-S displayed faster sulfur redox kinetics than PCNT-S. The difference in the formation energy between the bound Na₂S_x (1 ≤ x ≤ 4) on MoC/Mo₂C and the liquid state increases as x decreases. A strong binding of Na₂S_x (1 ≤ x ≤ 4) on MoC/Mo₂C surfaces results from a favorable charge transfer between the sulfur and Mo sites on the surface of carbides, as

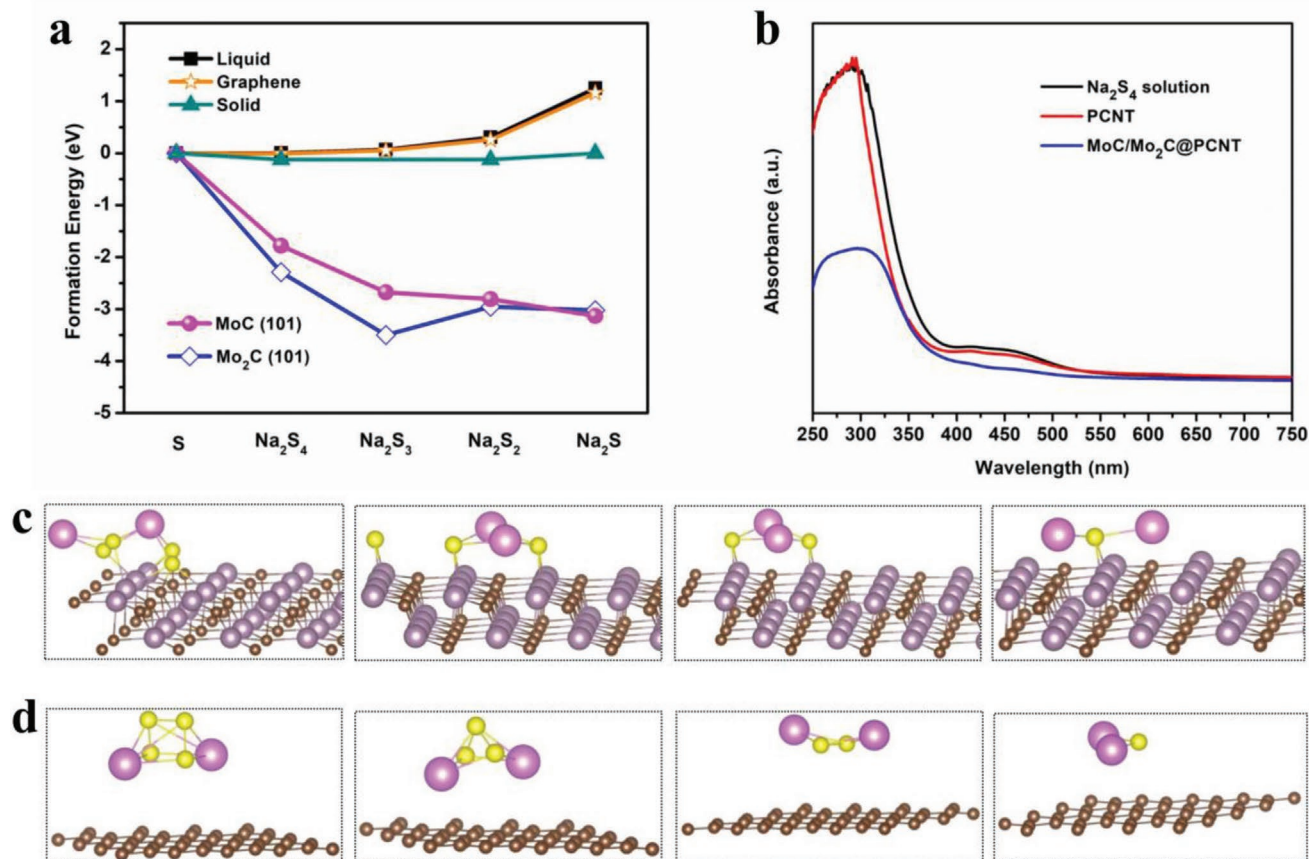


Figure 6. a) DFT calculated formation energy of Na_2S_x phases per mol of S. The energy of “solid” Na_2S_x structures are shown in blue using solid Na_2S ($x = 1$) and S_8 (left point) as the reference. The energy of bound molecular Na_2S_x to $\text{Mo}_2\text{C}(101)$ surface in shown in blue, $\text{MoC}(101)$ in purple, graphene in orange, and the free “liquid” state (black). b) UV-vis spectra of the Na_2S_4 blank solution, and the solutions after 1 h exposure to PCNT and $\text{MoC}/\text{Mo}_2\text{C}@PCNT$. c,d) Lowest energy configuration of Na_2S_x ($1 \leq x \leq 4$) on (c) $\text{MoC}(101)$ and (d) graphene surface using implicit solvation. Color scheme: carbon (brown), sodium (pink), sulfur (yellow), molybdenum (purple).

shown in Figure 6c and Figures S34 and S35 (Supporting Information). Within the binding configuration, electronic charge is transferred from Mo sites to sulfur. Table S4 (Supporting Information) shows the calculated Bader electronic charges on Mo sites in $\text{MoC}/\text{Mo}_2\text{C}$.^[56] Among the two carbides, Mo_2C binds the Na_2S_x ($1 \leq x \leq 4$) stronger to the corresponding surface as compared to MoC (Figure 6a), since Mo sites in Mo_2C exhibit a greater charge transfer to the sulfur sites. There is no binding formed between Na_2S_x and graphene, as revealed by Figure 6d. Moreover, the difference in the formation energy (≈ 3 eV) of (poly)sulfides between the solid phase and $\text{MoC}/\text{Mo}_2\text{C}$ would further suggest a large overpotential to form the solid crystalline phase from molecular phase. Beyond the thermodynamic constraints, the large surface area of the host itself determines the highly dispersed molecular state of either sulfur or Na_2S_x ($1 \leq x \leq 4$), which is in agreement with the XRD result of discharged products where negligible $\text{Na}_2\text{S}/\text{Na}_2\text{S}_2$ solid phases can be detected (Figure S36, Supporting Information).

The Na_2S_4 adsorption test was further conducted to demonstrate the strong affinity of $\text{MoC}/\text{Mo}_2\text{C}$ for Na_2S_x . Figure 6b shows the UV-vis absorption spectra of Na_2S_4 blank solution, and the solutions after 1 h exposure to PCNT and $\text{MoC}/\text{Mo}_2\text{C}@PCNT$. The original absorption peaks of the Na_2S_4

solution at 300 and 450 nm obviously decline after exposure to $\text{MoC}/\text{Mo}_2\text{C}@PCNT$, while PCNT baseline shows little Na_2S_4 adsorption. This is in accordance with the DFT simulation results. As Na_2S_2 and Na_2S on $\text{MoC}/\text{Mo}_2\text{C}$ display lower energies than the configuration of Na_2S_4 on $\text{MoC}/\text{Mo}_2\text{C}$, the two carbides can further catalyze the conversion of Na_2S_4 to Na_2S_2 and Na_2S .

3. Conclusions

Room-temperature sodium-metal-sulfur batteries are hindered by the slow reaction kinetics of sulfur and the uncontrolled dissolution of polysulfide species. Here, a novel molybdenum carbide ($\text{MoC}/\text{Mo}_2\text{C}$) electrocatalyst is first applied to promote Na-S reaction kinetics and anchor sulfur species. A facile single step achieves the combined catalyst-formation-host-activation process, leading to a composite host of the $\text{MoC}/\text{Mo}_2\text{C}$ in situ grown on nanoporous nitrogen-doped carbon nanotubes. Sulfur impregnation at 50% mass loading results in unique triphasic architecture, termed “ $\text{MoC}/\text{Mo}_2\text{C}@PCNT\text{-S}$.” The synergistic $\text{MoC}/\text{Mo}_2\text{C}$ electrocatalyst and carbon nanoporosity allow for the facile and efficient sulfur utilization following a

quasi-solid-phase transformation process, therefore contributing to the state-of-the-art electrochemical performance in carbonate electrolyte. For example, the MoC/Mo₂C@PCNT-S electrode delivers promising rate capabilities of 987 mAh g⁻¹ at 1 A g⁻¹, 818 mAh g⁻¹ at 3 A g⁻¹, and 621 mAh g⁻¹ at 5 A g⁻¹. The superior cycling stability is also obtained for the MoC/Mo₂C@PCNT-S electrode, even with high mass loading up to 13.0 mg cm⁻². The promotion in sulfur redox kinetics by MoC/Mo₂C loading is further reflected by the decreases in reaction polarization, Tafel slope value, and charge-transfer resistance of Na-S cells. Complementary DFT simulation provides fundamental insight regarding the electrocatalytic role of MoC/Mo₂C nanoparticles. Ascribed to the charge transfer between the sulfur and Mo sites on the surface of carbides, the formation energy of Na₂S_x (1 ≤ x ≤ 4) on MoC/Mo₂C is greatly lowered as compared to the case of baseline ordered carbon.

Supporting Information

Supporting Information is available from the Wiley Online Library or from the author.

Acknowledgements

P.L. and D.M. (conception and guidance of research, experimental work, preparation of paper) were supported by the Energy Storage Program, Office of Electricity (Grant Number: DE-AC05 00OR22725). H.H. and Y.W. (experimental work) were supported by the National Science Foundation, Division of Materials Research, Award Number 1938833. This research used resources of the Center for Functional Nanomaterials (CFN), which is a U.S. Department of Energy Office of Science User Facility, at Brookhaven National Laboratory under Contract No. DE-SC0012704. The computational work was supported by the Welch Foundation (F-1841) and National Energy Research Scientific Computing Center (NERSC).

Conflict of Interest

The authors declare no conflict of interest.

Data Availability Statement

The data that support the findings of this study are available from the corresponding author upon reasonable request.

Keywords

electrocatalysis, molybdenum carbide catalyst, Na-S batteries, porous carbon

Received: August 20, 2021
Revised: March 30, 2022
Published online: May 23, 2022

- [1] a) J. B. Goodenough, K. S. Park, *J. Am. Chem. Soc.* **2013**, *135*, 1167; b) M. Li, J. Lu, Z. Chen, K. Amine, *Adv. Mater.* **2018**, *30*, 1800561.
[2] Y. Wang, D. Zhou, V. Palomares, D. Shanmukaraj, B. Sun, X. Tang, C. Wang, M. Armand, T. Rojo, G. Wang, *Energy Environ. Sci.* **2020**, *13*, 3848.

- [3] a) Y. Wang, Y. Lai, J. Chu, Z. Yan, Y.-X. Wang, S.-L. Chou, H.-K. Liu, S. X. Dou, X. Ai, H. Yang, Y. Cao, *Adv. Mater.* **2021**, *33*, 2100229; b) M. K. Aslam, I. D. Seymour, N. Katyal, S. Li, T. Yang, S. J. Bao, G. Henkelman, M. Xu, *Nat. Commun.* **2020**, *11*, 5242; c) Z. Yan, Y. Liang, W. Hua, X. G. Zhang, W. Lai, Z. Hu, W. Wang, J. Peng, S. Indris, Y. Wang, S. L. Chou, H. Liu, S. X. Dou, *ACS Nano* **2020**, *14*, 10284; d) Z. Yan, Y. Liang, J. Xiao, W. Lai, W. Wang, Q. Xia, Y. Wang, Q. Gu, H. Lu, S. L. Chou, Y. Liu, H. Liu, S. X. Dou, *Adv. Mater.* **2020**, *32*, 1906700; e) H. Liu, W. H. Lai, Y. Liang, X. Liang, Z. C. Yan, H. L. Yang, Y. J. Lei, P. Wei, S. Zhou, Q. F. Gu, S. L. Chou, H. K. Liu, S. X. Dou, Y. X. Wang, *J. Mater. Chem. A* **2021**, *9*, 566; f) Y. X. Wang, B. Zhang, W. Lai, Y. Xu, S. L. Chou, H. K. Liu, S. X. Dou, *Adv. Energy Mater.* **2017**, *7*, 1602829; g) H. Li, M. Zhao, B. Jin, Z. Wen, H. K. Liu, Q. Jiang, *Small* **2020**, *16*, 1907464; h) A. Ghosh, A. Kumar, T. Das, A. Ghosh, S. Chakraborty, M. Kar, D. R. MacFarlane, S. Mitra, *Adv. Funct. Mater.* **2020**, *30*, 2005669; i) B. Guo, W. Du, T. Yang, J. Deng, D. Liu, Y. Qi, J. Jiang, S. J. Bao, M. Xu, *Adv. Sci.* **2020**, *7*, 1902617; j) W. Bao, C. E. Shuck, W. Zhang, X. Guo, Y. Gogotsi, G. Wang, *ACS Nano* **2019**, *13*, 11500; k) W. H. Lai, H. Wang, L. Zheng, Q. Jiang, Z. C. Yan, L. Wang, H. Yoshikawa, D. Matsumura, Q. Sun, Y. X. Wang, Q. Gu, J. Z. Wang, H. K. Liu, S. L. Chou, S. X. Dou, *Angew. Chem., Int. Ed.* **2020**, *59*, 22171.
[4] Y. Wang, W. Lai, S. Chou, H. Liu, S. Dou, *Adv. Mater.* **2019**, *32*, 1903952.
[5] a) X. Hong, J. Mei, L. Wen, Y. Tong, A. J. Vasileff, L. Wang, J. Liang, Z. Sun, S. X. Dou, *Adv. Mater.* **2019**, *31*, 1802822; b) Q. Zou, Z. Liang, G. Y. Du, C. Y. Liu, E. Y. Li, Y. C. Lu, *J. Am. Chem. Soc.* **2018**, *140*, 10740.
[6] X. Yu, A. Manthiram, *ChemElectroChem* **2014**, *1*, 1275.
[7] a) H. Zhang, T. Diemant, B. Qin, H. Li, R. J. Behm, S. Passerini, *Energies* **2020**, *13*, 836; b) I. Bauer, M. Kohl, H. Althues, S. Kaskel, *Chem. Commun.* **2014**, *50*, 3208; c) X. Huo, Y. Liu, R. Li, J. Li, *Ionics* **2019**, *25*, 5373.
[8] a) Y. M. Chen, W. Liang, S. Li, F. Zou, S. M. Bhowmik, Z. Qiang, M. Gao, B. D. Vogt, Y. Zhu, *J. Mater. Chem. A* **2016**, *4*, 12471; b) J. Mou, Y. Li, T. Liu, W. Zhang, M. Li, Y. Xu, L. Zhong, W. Pan, C. Yang, J. Huang, M. Liu, *Small Methods* **2021**, *5*, 2100455; c) F. Xiao, H. Wang, J. Xu, W. Yang, X. Yang, D. Y. W. Yu, A. L. Rogach, *Adv. Energy Mater.* **2021**, *11*, 2100989; d) C. Ye, Y. Jiao, D. Chao, T. Ling, J. Shan, B. Zhang, Q. Gu, K. Davey, H. Wang, S. Z. Qiao, *Adv. Mater.* **2020**, *32*, 1907557; e) F. Xiao, X. Yang, H. Wang, J. Xu, Y. Liu, D. Y. W. Yu, A. L. Rogach, *Adv. Energy Mater.* **2020**, *10*, 2000931.
[9] Y. X. Wang, J. Yang, W. Lai, S. L. Chou, Q. F. Gu, H. K. Liu, D. Zhao, S. X. Dou, *J. Am. Chem. Soc.* **2016**, *138*, 16576.
[10] Z. Yan, J. Xiao, W. Lai, L. Wang, F. Gebert, Y. Wang, Q. Gu, H. Liu, S. L. Chou, H. Liu, S. X. Dou, *Nat. Commun.* **2019**, *10*, 4793.
[11] H. Wang, Z. Tong, R. Yang, Z. Huang, D. Shen, T. Jiao, X. Cui, W. Zhang, Y. Jiang, C. S. Lee, *Adv. Energy Mater.* **2019**, *9*, 1903046.
[12] A. Kumar, A. Ghosh, A. Roy, M. R. Panda, M. Forsyth, D. R. MacFarlane, S. Mitra, *Energy Storage Mater.* **2019**, *20*, 196.
[13] D. Ma, Y. Li, J. Yang, H. Mi, S. Luo, L. Deng, C. Yan, M. Rauf, P. Zhang, X. Sun, X. Ren, J. Li, H. Zhang, *Adv. Funct. Mater.* **2018**, *28*, 1705537.
[14] T. Yang, B. Guo, W. Du, M. K. Aslam, M. Tao, W. Zhong, Y. Chen, S.-J. Bao, X. Zhang, M. Xu, *Adv. Sci.* **2019**, *6*, 1901557.
[15] C. Dong, H. Zhou, B. Jin, W. Gao, X. Lang, J. Li, Q. Jiang, *J. Mater. Chem. A* **2021**, *9*, 3451.
[16] N. Wang, Y. Wang, Z. Bai, Z. Fang, X. Zhang, Z. Xu, Y. Ding, X. Xu, Y. Du, S. Dou, G. Yu, *Energy Environ. Sci.* **2020**, *13*, 562.
[17] B. W. Zhang, T. Sheng, Y. D. Liu, Y. X. Wang, L. Zhang, W. H. Lai, L. Wang, J. Yang, Q. F. Gu, S. L. Chou, H. K. Liu, S. X. Dou, *Nat. Commun.* **2018**, *9*, 4082.
[18] S. Luo, J. Ruan, Y. Wang, J. Hu, Y. Song, M. Chen, L. Wu, *Small* **2021**, *17*, 2101879.

- [19] Z. Huang, B. Song, H. Zhang, F. Feng, W. Zhang, K. Lu, Q. Chen, *Adv. Funct. Mater.* **2021**, *31*, 2100666.
- [20] a) Y. Li, S. Yao, C. Zhang, Y. He, Y. Wang, Y. Liang, X. Shen, T. Li, S. Qin, W. Wen, *Int. J. Energy Res.* **2020**, *44*, 8388; b) H. Shi, Z. Sun, W. Lv, S. Wang, Y. Shi, Y. Zhang, S. Xiao, H. Yang, Q. H. Yang, F. Li, *J. Mater. Chem. A* **2019**, *7*, 11298; c) H. Dai, L. Wang, Y. Zhao, J. Xue, R. Zhou, C. Yu, J. An, J. Zhou, Q. Chen, G. Sun, W. Huang, *Research* **2021**, *2021*, 5130420.
- [21] H. Hao, T. Hutter, B. L. Boyce, J. Watt, P. Liu, D. Mitlin, *Chem. Rev.* **2022**, *122*, 8053.
- [22] C. Bommier, D. Mitlin, X. Ji, *Prog. Mater. Sci.* **2018**, *97*, 170.
- [23] B. Lee, E. Paek, D. Mitlin, S. W. Lee, *Chem. Rev.* **2019**, *119*, 5416.
- [24] H. Liu, W. H. Lai, Y. Lei, H. Yang, N. Wang, S. Chou, H. K. Liu, S. X. Dou, Y. X. Wang, *Adv. Energy Mater.* **2022**, *12*, 2103304.
- [25] D. Zhou, Y. Chen, B. Li, H. Fan, F. Cheng, D. Shanmukaraj, T. Rojo, M. Armand, G. Wang, *Angew. Chem., Int. Ed.* **2018**, *57*, 10168.
- [26] D. Zhou, X. Tang, X. Guo, P. Li, D. Shanmukaraj, H. Liu, X. Gao, Y. Wang, T. Rojo, M. Armand, G. Wang, *Angew. Chem., Int. Ed.* **2020**, *59*, 16725.
- [27] X. Xu, D. Zhou, X. Qin, K. Lin, F. Kang, B. Li, D. Shanmukaraj, T. Rojo, M. Armand, G. Wang, *Nat. Commun.* **2018**, *9*, 3870.
- [28] a) F. Ma, Y. Wan, X. Wang, X. Wang, J. Liang, Z. Miao, T. Wang, C. Ma, G. Lu, J. Han, Y. Huang, Q. Li, *ACS Nano* **2020**, *14*, 10115; b) J. Q. Chi, X. Shang, S. S. Lu, B. Dong, Z. Z. Liu, K. L. Yan, W. K. Gao, Y. M. Chai, C. G. Liu, *Carbon* **2017**, *124*, 555; c) Z. Shi, K. Nie, Z. J. Shao, B. Gao, H. Lin, H. Zhang, B. Liu, Y. Wang, Y. Zhang, X. Sun, X. M. Cao, P. Hu, Q. Gao, Y. Tang, *Energy Environ. Sci.* **2017**, *10*, 1262; d) J.-Q. Chi, W.-K. Gao, J.-H. Lin, B. Dong, J.-F. Qin, Z.-Z. Liu, B. Liu, Y.-M. Chai, C.-G. Liu, *J. Catal.* **2018**, *360*, 9; e) M. Ji, S. Niu, Y. Du, B. Song, P. Xu, *ACS Sustainable Chem. Eng.* **2018**, *6*, 11922.
- [29] Y. J. Oh, J. H. Kim, J. Y. Lee, S. K. Park, Y. C. Kang, *Chem. Eng. J.* **2020**, *384*, 123344.
- [30] a) J. S. Cho, J. K. Lee, Y. C. Kang, *Sci. Rep.* **2016**, *6*, 23699; b) D. Xu, C. Chen, J. Xie, B. Zhang, L. Miao, J. Cai, Y. Huang, L. Zhang, *Adv. Energy Mater.* **2016**, *6*, 1501929; c) J. Yang, X. Zhou, D. Wu, X. Zhao, Z. Zhou, *Adv. Mater.* **2017**, *29*, 1604108; d) J. H. Choi, S. K. Park, Y. C. Kang, *Small* **2019**, *15*, 1803043; e) J. Ding, H. Wang, Z. Li, K. Cui, D. Karpuzov, X. Tan, A. Kohandehghan, D. Mitlin, *Energy Environ. Sci.* **2015**, *8*, 941; f) J. Ding, H. L. Wang, Z. Li, A. Kohandehghan, K. Cui, Z. W. Xu, B. Zahiri, X. H. Tan, E. M. Lotfabad, B. C. Olsen, D. Mitlin, *ACS Nano* **2013**, *7*, 11004; g) H. Wang, Z. W. Xu, A. Kohandehghan, Z. Li, K. Cui, X. H. Tan, T. J. Stephenson, C. K. King'ondeu, C. M. B. Holt, B. C. Olsen, J. K. Tak, D. Harfield, A. O. Anyia, D. Mitlin, *ACS Nano* **2013**, *7*, 5131; h) E. M. Lotfabad, J. Ding, K. Cui, A. Kohandehghan, W. P. Kalisvaart, M. Hazelton, D. Mitlin, *ACS Nano* **2014**, *8*, 7115.
- [31] a) E. Markevich, G. Salitra, Y. Talyosef, F. Chesneau, D. Aurbach, *J. Electrochem. Soc.* **2017**, *164*, A6244; b) Q. Guo, S. Li, X. Liu, H. Lu, X. Chang, H. Zhang, X. Zhu, Q. Xia, C. Yan, H. Xia, *Adv. Sci.* **2020**, *7*, 1903246.
- [32] A. Y. S. Eng, Y. Wang, D. T. Nguyen, S. Y. Tee, C. Y. J. Lim, X. Y. Tan, M. F. Ng, J. Xu, Z. W. Seh, *Nano Lett.* **2021**, *21*, 5401.
- [33] S. Wei, S. Xu, A. Agrawal, S. Choudhury, Y. Lu, Z. Tu, L. Ma, L. A. Archer, *Nat. Commun.* **2016**, *7*, 11722.
- [34] a) J. He, W. Lv, Y. Chen, J. Xiong, K. Wen, C. Xu, W. Zhang, Y. Li, W. Qin, W. He, *J. Mater. Chem. A* **2018**, *6*, 10466; b) H. Yang, S. Zhou, B. Zhang, S. Chu, H. Guo, Q. Gu, H. Liu, Y. Lei, K. Konstantinov, Y. Wang, S. Chou, H. Liu, S. Dou, *Adv. Funct. Mater.* **2021**, *31*, 2102280.
- [35] X. Zhang, J. Wang, T. Guo, T. Liu, Z. Wu, L. Cavallo, Z. Cao, D. Wang, *Appl. Catal., B* **2019**, *247*, 78.
- [36] H. M. Jo, Y. Kim, D. H. Youn, *J. Alloys Compd.* **2021**, *855*, 157420.
- [37] C. Wu, Y. Lei, L. Simonelli, D. Tonti, A. Black, X. Lu, W. H. Lai, X. Cai, Y. X. Wang, Q. Gu, S. L. Chou, H. K. Liu, G. Wang, S. X. Dou, *Adv. Mater.* **2022**, *34*, 2108363.
- [38] a) X. M. Zhao, Q. Zhu, S. D. Xu, L. Chen, Z. J. Zuo, X. M. Wang, S. B. Liu, D. Zhang, *J. Electroanal. Chem.* **2019**, *832*, 392; b) S. Zhang, Y. Yao, X. Jiao, M. Ma, H. Huang, X. Zhou, L. Wang, J. Bai, Y. Yu, *Adv. Mater.* **2021**, *33*, 2103846.
- [39] a) H. G. Lee, J. T. Lee, K. Eom, *Adv. Sustainable Syst.* **2018**, *2*, 1800076; b) D. Liu, Z. Li, X. Li, X. Chen, Z. Li, L. Yuan, Y. Huang, *ACS Appl. Mater. Interfaces* **2022**, *14*, 6658.
- [40] M. R. Busche, P. Adelhelm, H. Sommer, H. Schneider, K. Leitner, J. Janek, *J. Power Sources* **2014**, *259*, 289.
- [41] H. Kim, J. T. Lee, G. Yushin, *J. Power Sources* **2013**, *226*, 256.
- [42] Y. V. Mikhaylik, J. R. Akridge, *J. Electrochem. Soc.* **2004**, *151*, A1969.
- [43] a) A. Y. S. Eng, V. Kumar, Y. Zhang, J. Luo, W. Wang, Y. Sun, W. Li, Z. W. Seh, *Adv. Energy Mater.* **2021**, *11*, 2003493; b) Y. Wang, H. Dong, N. Kataly, H. Hao, P. Liu, H. Celio, G. Henkelman, J. Watt, D. Mitlin, *Adv. Mater.* **2022**, *34*, 2106005.
- [44] a) K. Chen, H. Li, Y. Xu, K. Liu, H. Li, X. Xu, X. Qiu, M. Liu, *Nanoscale* **2019**, *11*, 5967; b) X. Wu, A. Markir, Y. Xu, E. C. Hu, K. T. Dai, C. Zhang, W. Shin, D. P. Leonard, K. I. Kim, X. Ji, *Adv. Energy Mater.* **2019**, *9*, 1902422.
- [45] S. Xin, Y. X. Yin, Y. G. Guo, L. J. Wan, *Adv. Mater.* **2014**, *26*, 1261.
- [46] a) B. Yu, A. Huang, D. Chen, K. Srinivas, X. Zhang, X. Wang, B. Wang, F. Ma, C. Liu, W. Zhang, J. He, Z. Wang, Y. Chen, *Small* **2021**, *17*, 2100460; b) J. He, A. Bhargava, H. Y. Asl, Y. Chen, A. Manthiram, *Adv. Energy Mater.* **2020**, *10*, 2001017.
- [47] a) Y. Qi, Q. J. Li, Y. Wu, S. J. Bao, C. Li, Y. Chen, G. Wang, M. Xu, *Nat. Commun.* **2021**, *12*, 6347; b) M. Cuisinier, C. Hart, M. Balasubramanian, A. Garsuch, L. F. Nazar, *Adv. Energy Mater.* **2015**, *5*, 1401801; c) H. L. Wu, L. A. Huff, A. A. Gewirth, *ACS Appl. Mater. Interfaces* **2015**, *7*, 1709.
- [48] a) Y. Li, C. Wang, W. Wang, A. Y. S. Eng, M. Wan, L. Fu, E. Mao, G. Li, J. Tang, Z. W. Seh, Y. Sun, *ACS Nano* **2020**, *14*, 1148; b) J. He, G. Hartmann, M. Lee, G. S. Hwang, Y. Chen, A. Manthiram, *Energy Environ. Sci.* **2019**, *12*, 344.
- [49] a) S. Li, Z. Han, W. Hu, L. Peng, J. Yang, L. Wang, Y. Zhang, B. Shan, J. Xie, *Nano Energy* **2019**, *60*, 153; b) K. Xu, X. Liu, J. Liang, J. Cai, K. Zhang, Y. Lu, X. Wu, M. Zhu, Y. Liu, Y. Zhu, G. Wang, Y. Qian, *ACS Energy Lett.* **2018**, *3*, 420.
- [50] D. Aurbach, K. Gamolsky, B. Markovsky, Y. Gofer, M. Schmidt, U. Heide, *Electrochim. Acta* **2002**, *47*, 1423.
- [51] a) S. Zhang, G. Wang, B. Wang, J. Wang, J. Bai, H. Wang, *Adv. Funct. Mater.* **2020**, *30*, 2001592; b) E. Zhang, X. Jia, B. Wang, J. Wang, X. Yu, B. Lu, *Adv. Sci.* **2020**, *7*, 2000470; c) L. Tao, Y. Yang, H. Wang, Y. Zheng, H. Hao, W. Song, J. Shi, M. Huang, D. Mitlin, *Energy Storage Mater.* **2020**, *27*, 212; d) X. Ge, H. Di, P. Wang, X. Miao, P. Zhang, H. Wang, J. Ma, L. Yin, *ACS Nano* **2020**, *14*, 16022.
- [52] H. Tian, H. Tian, S. Wang, S. Chen, F. Zhang, L. Song, H. Liu, J. Liu, G. Wang, *Nat. Commun.* **2020**, *11*, 5025.
- [53] T. Brezesinski, J. Wang, S. H. Tolbert, B. Dunn, *Nat. Mater.* **2010**, *9*, 146.
- [54] V. H. Pham, J. A. Boscoboinik, D. J. Stacchiola, E. C. Self, P. Manikandan, S. Nagarajan, Y. Wang, V. G. Pol, J. Nanda, E. Paek, D. Mitlin, *Energy Storage Mater.* **2019**, *20*, 71.
- [55] Q. Zhang, Y. Wang, Z. W. Seh, Z. Fu, R. Zhang, Y. Cui, *Nano Lett.* **2015**, *15*, 3780.
- [56] G. Henkelman, A. Arnaldsson, H. Jónsson, *Comput. Mater. Sci.* **2006**, *36*, 354.